



**HAL**  
open science

## Structural and mechanistic basis for RiPP epimerization by a radical SAM enzyme

Xavier Kubiak, Ivan Polsinelli, Leonard Chavas, Cameron Fyfe, Alain Guillot,  
Laura Fradale, Clémence Brewée, Stéphane Grimaldi, Guillaume Gerbaud,  
Aurélien Thureau, et al.

► **To cite this version:**

Xavier Kubiak, Ivan Polsinelli, Leonard Chavas, Cameron Fyfe, Alain Guillot, et al.. Structural and mechanistic basis for RiPP epimerization by a radical SAM enzyme. *Nature Chemical Biology*, inPress, 10.1038/s41589-023-01493-1 . hal-04371487

**HAL Id: hal-04371487**

**<https://hal.science/hal-04371487>**

Submitted on 16 Feb 2024

**HAL** is a multi-disciplinary open access archive for the deposit and dissemination of scientific research documents, whether they are published or not. The documents may come from teaching and research institutions in France or abroad, or from public or private research centers.

L'archive ouverte pluridisciplinaire **HAL**, est destinée au dépôt et à la diffusion de documents scientifiques de niveau recherche, publiés ou non, émanant des établissements d'enseignement et de recherche français ou étrangers, des laboratoires publics ou privés.

1 **Editor summary:**

2 Peptide epimerization is a common but enigmatic post-translational modification  
3 found in antibiotics formed from ribosomally-synthesized and post-  
4 translationally modified peptides. Now, crystallographic snapshots,  
5 spectroscopy and biochemical investigations, have provided insight into the  
6 mechanism of peptide epimerization catalyzed by radical SAM epimerases.

7  
8

9 **Peer Review Information:**

10

11 *Nature Chemical Biology* thanks Qi Zhang and the other, anonymous reviewers  
12 for their contribution to the peer review of this work.

13  
14  
15  
16  
17  
18

**1. Extended Data**

Figure or Table #	Figure/Table title	Filename	Figure/Table Legend
Please group Extended Data items by type, in sequential order. Total number of items (Figs. + Tables) must not exceed 10.	One sentence only	Whole original file name including extension. i.e.: Smith_ED_Fig1.jpg	If you are citing a reference for the first time in these legends, please include all new references in the main text Methods References section, and carry on the numbering from the main References section of the paper. If your paper does not have a Methods section, include all new references at the end of the main Reference list.
Extended Data Fig. 1	<b>Topology diagram of EpeE, radical SAM binding motifs and coordination of SAM in EpeE and representative members of the radical SAM enzyme superfamily.</b>	ED_Figure1.jpg	<b>a</b> , EpeE topology diagram showing a truncated $\alpha 5/\beta 6$ TIM barrel in the radical SAM domain and T-SPASM domain with a single AuxI cluster. The binding region is depicted in bold line. The position of the [4Fe-4S] clusters (yellow and orange) and the coordinating cysteine residues (yellow) are indicated. <b>b</b> , Radical SAM cluster of EpeE in interaction with SAH. Residues from the conserved: GGE, GXIXGXXE, ribose, $\beta 6$ and CX <sub>3</sub> CX $\Phi$ C motifs are colored according to their domain in EpeE (radical SAM domain). The unusual His-20 residue from the CX <sub>3</sub> CX $\Phi$ C motif is highlighted. Hydrogen-bonds are shown with black lines, radical SAM [4Fe-4S] cluster with yellow and orange sticks and SAH with green sticks. <b>c</b> , The CX <sub>3</sub> CX $\Phi$ C motif of structurally characterized members of the radical SAM superfamily of enzymes. The $\Phi$ residue is: Tyr in AnSME (green sticks) and CteB (brown sticks); Phe in SkfB (yellow sticks) and SuiB (violet sticks); Met

			in NosL (white sticks). As for CteB, the side chain of the $\Phi$ amino acid coordinates both the adenine and the ribose moiety, but only EpeE makes two H-bonds with the N6 and N7 of the adenine moiety.
Extended Data Fig. 2	<b>Interactions stabilizing the T-SPASM domain and the bridging region of EpeE.</b>	ED_Figure2.jpg	<b>a</b> , Overall structure of EpeE highlighting the bridging region (red cartoon) between EpeE domains (radical SAM domain in light blue, T-SPASM in teal). <b>b</b> , The bridging region (red cartoon) makes extensive H-bonds (black dotted lines) with $\alpha 3'$ helix and $\alpha 3'$ - $\alpha 4'$ loop (green cartoon) (left panel). The C-terminal helix $\alpha 5'$ is stabilized by $\alpha 3'$ helix through H-bond and hydrophobic interactions (right panel). <b>c</b> , Comparison between the twitch and SPASM-domains of representative radical SAM enzymes. Similarly to twitch radical SAM enzymes (SkfB & BtrN), EpeE coordinates a single [4Fe-4S] cluster, however, the bridging region extends toward the location of AuxII cluster found in SPASM enzymes (AnSME, CteB & SuiB). The C-terminal $\alpha 5'$ helix of EpeE, absent in twitch-domains, is displaced at the opposite side of the AuxI cluster compared to the C-terminal $\alpha 6'$ helix of SPASM-domain enzymes AnSME and CteB which lies against the $\alpha 6$ helix of the TIM barrel (missing in EpeE). Only the AuxI cluster, $\beta 1'$ - $\beta 2'$ anti-parallel sheets and $\alpha 2'$ helix positions are conserved in all enzymes. The TIM barrel domain is colored in white. The Twitch/SPASM domains are colored by protein. The AuxI and II clusters are shown in yellow and orange sticks.
Extended Data Fig. 3	<b>EPR, UV-visible and HYSCORE analysis of EpeE in absence or presence of SAM.</b>	ED_Figure3.jpg	<b>a</b> , Temperature dependence of EPR spectra of dithionite-reduced reconstituted samples of wild-type EpeE in the absence (left panel) or in the presence (right panel) of a 5-fold stoichiometric excess of SAM. The microwave power was adjusted at each temperature to avoid saturation effects. Spectra have been amplitude-normalized. Number of accumulations: 4. The signal of the SAM-bound [4Fe-4S] <sup>+</sup> cluster relaxes significantly faster than the one detected in the unbound form. Indeed, the former broadens at temperatures above 6 K and is no longer visible at 30 K and above (right panel) whereas the latter is still detected without significant broadening at 30 K (left panel). Such differences in the relaxation behavior of the two forms allowed us to reveal partial conversion between these forms upon addition of SAM. Indeed, a weak contribution of the unbound form is detected in the sample incubated with a 5-fold excess of SAM when measured at 30 K (right panel). <b>b</b> , Power saturation experiments of dithionite-reduced reconstituted samples of wild-type EpeE in

			<p>the absence (upper panel) or in the presence (lower panel) of a 5-fold stoichiometric excess of SAM. Peak-to-peak amplitudes between features measured as indicated by arrows on left spectra are plotted against square root of microwave power in a log-log plot (blue filled circles). The dotted line represents the non-saturation regime for which the EPR amplitude is proportional to the square root of the microwave power. Other experimental conditions: temperature, 15 K (upper panel) or 6 K (lower panel), microwave power, 0.1 mW (left spectra), number of accumulations, 4. <b>c</b>, UV visible analysis of EpeE wild-type (upper panel) and A3-mutant (lower panel). Before (grey line) and after (black line) anaerobic FeS cluster reconstitution. <b>d</b>, X-band HYSCORE spectra of dithionite-reduced reconstituted samples of wild-type EpeE in the presence (upper panel) or in the absence (lower panel) of a 5-fold stoichiometric excess of SAM. Only the low frequency region is shown. Experimental conditions are given in the Methods section. The low frequency region of the HYSCORE spectrum of the anaerobically reduced and reconstituted wild type enzyme in the presence of SAM displays a complex set of signals in both the (+, +) and (-, +) quadrants which can be unambiguously assigned to a hyperfine coupling to a <math>^{14}\text{N}</math> nucleus in the intermediate coupling regime for which the isotropic part of the hyperfine coupling constant <math>a_{\text{iso}}</math> is nearly equal to twice the <math>^{14}\text{N}</math> Larmor frequency, i.e. <math>\nu_l(^{14}\text{N}) \approx 1.1</math> MHz (upper panel). These signals are absent in the corresponding HYSCORE spectrum of the enzyme prepared in the same conditions but without SAM (lower panel).</p>
Extended Data Fig. 4	LC-MS analysis of EpeE incubated with peptides 4, 5, 6 & 7.	ED_Figure4.jpg	<p>Activity of EpeE with peptide 4 (a), 5 (b), 6 (c) and 7 (d) was assayed in deuterated buffer. LC-MS analysis of peptide at T0 (upper left panel) and after 90 min incubation under anaerobic conditions (lower left panel). Comparison between the mass spectrum of the substrate (upper middle panel) and the product (lower middle panel) showed a +1 Da mass increment, consistent with <math>^2\text{H}</math>-atom incorporation while mass spectrum analysis of the 5'-dA is shown in right panel.</p>
Extended Data Fig. 5	LC-MS/MS analysis of the peptide 4, 5, 6 and 7 and the reaction products formed after	ED_Figure5.jpg	<p><b>a</b>, Mass fragmentation spectrum of peptide 4 (upper panel) and the epimerized peptide product (lower panel). (<i>see Supplementary Tables 1 - 2 for full assignment</i>). <b>b</b>, Mass fragmentation spectrum of peptide 5 (upper panel) and the epimerized peptide product (lower panel). (<i>see Supplementary Tables 3 - 4 for full assignment</i>). <b>c</b>, Mass fragmentation</p>

	incubation with EpeE.		spectrum of peptide <b>6</b> (upper panel) and the epimerized peptide product (lower panel). ( <i>see Supplementary Tables 5 - 6 for full assignment</i> ). <b>d</b> , Mass fragmentation spectrum of peptide <b>7</b> (upper panel) and the epimerized peptide product (lower panel). ( <i>see Supplementary Tables 7 - 8 for full assignment</i> ). The relevant ions with a mass shift of +1 Da due to <sup>2</sup> H incorporation after reaction with EpeE are highlighted.
Extended Data Fig. 6	Comparison between substrate-free and peptide-bound structures of EpeE.	ED_Figure6.jpg	<b>a</b> , Superimposition of substrate-free and peptide-bound structures of EpeE. <b>b</b> , Close-up view showing the major structural movements including the $\alpha 3'$ - $\alpha 5'$ helices (indicated by arrows in panel a) of the SPASM-related domain. The substrate-free EpeE structure is shown in grey and the peptide-bound EpeE structure in pale cyan (chain A) and deep teal (chain B). Alignment of the substrate-free and -bound structures using all domains (634 residues) has a r.m.s.d. of 0.78 Å, as calculated using Coot SSM.
Extended Data Fig. 7	Peptide 5 bound in the active-site of wild-type EpeE structure.	ED_Figure7.jpg	<b>a</b> , The peptide <b>5</b> was built for 7 out of 11 residues (KENRWIL) according to the electron density. The omit map (blue mesh) of peptide <b>5</b> (in pink sticks) is contoured at 3 $\sigma$ . SAH is depicted in stick, the radical SAM [4Fe-4S] and AuxI clusters are shown as spheres. <b>b</b> , Peptide <b>5</b> fold. The peptide is shown in salmon (chain C) and orange (chain D) and colored by atom type. Intramolecular interactions are depicted in black dashed line.
Extended Data Fig. 8	Structures of C223A EpeE mutant bound with peptide 5 and 6.	ED_Figure8.jpg	<b>a</b> , Superimposition of EpeE WT in complex with peptide <b>5</b> (pale cyan) and EpeE <b>C223A</b> in complex with peptide <b>5</b> (bright orange; r.m.s.d. of 0.22 Å). <b>b</b> , Superimposition of EpeE WT in complex with peptide <b>5</b> (pale cyan) and EpeE <b>C223A</b> in complex with peptide <b>6</b> (green; r.m.s.d. of 0.23 Å). <b>c</b> , Close-up of EpeE <b>C223A</b> mutant active site. The peptide <b>5</b> (left panel) was built for 9 out of 11 residues (KSKENRWIL) according to the electron density. The peptide <b>6</b> (right panel) was built for all the 11 residues (KENRWILGSGH) according to the electron density. The omit maps (blue mesh) of peptide <b>5</b> (pink sticks) and <b>6</b> (purple sticks) are contoured at 3 $\sigma$ . SAH (green) is depicted in stick, the radical SAM [4Fe-4S] and AuxI clusters are shown as spheres. <b>d</b> , Structure of EpeE <b>C223A</b> mutant with peptide <b>6</b> in its active site. K171 and D143 are

			stacking H49 from peptide 6 (left panel) while, in the substrate-free WT EpeE structure, D143 and K171 have a distinct orientation stabilized by a salt bridge (right panel). <b>e</b> , The presence of H49 in the structure of EpeE C223A mutant with peptide 6 provided inter-chain interactions between the two enzyme subunits.
Extended Data Fig. 9	<b>The C223 residue in the structures of wild-type EpeE and D210A mutant.</b>	ED_Figure9.jpg	<b>a</b> , Interactions involving D210 in the structure of EpeE with peptide 5. D210 provides key electrostatic interactions to the substrate (residues N41 and R42) and is stabilized by a polar bond with the protein residue T5. The distance between C223 and D210 is 5.08 Å. <b>b</b> , <b>Orientations of C223 in the structure of the D210A EpeE mutant.</b> The omit map (blue mesh) of C223 in chain A (left panel) and chain B (right panel) is contoured at 3σ. C223 was modeled as a persulfurated cysteine residue. In chain A (left panel), C223 adopted two orientations.
Extended Data Table. 1	<b>Crystallographic data and refinement statistics</b>	Table_1.pdf	

19

20

## 21 1. Supplementary Information:

### 22 A. PDF Files

23

Item	Present?	Filename	A brief, numerical description of file contents.
		Whole original file name including extension. i.e.: Smith_SI.pdf. The extension must be .pdf	i.e.: <i>Supplementary Figures 1-4, Supplementary Discussion, and Supplementary Tables 1-4.</i>
Supplementary Information	Yes	Supplementary_Information.pdf	Supplementary Tables 1-10

Reporting Summary	Yes	nr-reporting-summary.pdf
Peer Review Information	No	OFFICE USE ONLY

24

## 25 2. Source Data

26

Parent Figure or Table	Filename	Data description
	Whole original file name including extension. i.e.: <i>Smith_SourceData_Fig1.xls</i> , or <i>Smith_Unmodified_Gels_Fig1.pdf</i>	i.e.: Unprocessed western Blots and/or gels, Statistical Source Data, etc.
Source Data Fig. 4	Source_data_file.csv	Statistical source data for Fig. 4b

27

28

## 29 Structural and mechanistic basis for RiPP epimerization by 30 a radical SAM enzyme

31

32 **Xavier Kubiak<sup>1+</sup>, Ivan Polsinelli<sup>1+</sup>, Leonard M. G. Chavas<sup>3+</sup>, Cameron D Fyfe<sup>1+</sup>,**  
33 **Alain Guillot<sup>1</sup>, Laura Fradale<sup>1</sup>, Clemence Brewee<sup>1</sup>, Stéphane Grimaldi<sup>4</sup>,**  
34 **Guillaume Gerbaud<sup>4</sup>, Aurélien Thureau<sup>2</sup>, Pierre Legrand<sup>2</sup>, Olivier Berteau<sup>1\*</sup> &**  
35 **Alhosna Benjdia<sup>1\*</sup>**

36 <sup>1</sup>Université Paris-Saclay, INRAE, AgroParisTech, Micalis Institute, ChemSyBio, 78350  
37 Jouy-en-Josas, France

38 <sup>2</sup>Synchrotron SOLEIL, HelioBio group, L'Orme des Merisiers, 91190 Gif sur-Yvette,  
39 France

40 <sup>3</sup>Nagoya University, Nagoya 464-8603, Japan.

41 <sup>4</sup>Aix Marseille Univ, CNRS, BIP, IM2B, IMM, Marseille, France

42

43 \*Corresponding authors. Email: [Olivier.Berteau@inrae.fr](mailto:Olivier.Berteau@inrae.fr); [Alhosna.Benjdia@inrae.fr](mailto:Alhosna.Benjdia@inrae.fr)

44 <sup>+</sup>Equal contribution

45 **D-amino acid residues have been reported in countless peptides and natural products**  
46 **including ribosomally-synthesized and post-translationally modified peptides (RiPPs),**  
47 **where they are critical for the bioactivity of several antibiotics and toxins. Recently,**  
48 **radical S-adenosyl-L-methionine (SAM) enzymes have emerged as the only biocatalysts**

49 **capable of installing direct and irreversible epimerization in RiPPs. However, the**  
50 **mechanism underpinning this biochemical process is ill-understood and the structural**  
51 **basis for this post-translational modification remains unknown. Here we report an**  
52 **atomic-resolution crystal structure of a radical SAM RiPP-modifying enzyme in complex**  
53 **with its substrate properly positioned in the active site. Crystallographic snapshots,**  
54 **SEC-SAXS, EPR spectroscopy and biochemical analyses revealed how epimerizations**  
55 **are installed in RiPPs and support a unprecedented enzyme mechanism for peptide**  
56 **epimerization. Collectively, our study brings unique perspectives on how radical SAM**  
57 **enzymes interact with RiPPs and catalyze post-translational modifications in natural**  
58 **products.**



## 59 Introduction

60 Ribosomally-synthesized and post-translationally modified peptides (RiPPs) form one of the  
61 major families of natural products<sup>1,2</sup>. They have recently attracted considerable interest  
62 because of their involvement in the homeostasis of the human microbiota<sup>2-6</sup> and their potential  
63 to develop innovative antibiotics<sup>7-9</sup>. The biosynthesis of RiPPs usually follows a simple logic  
64 with the translation of a precursor peptide containing a leader or a follower sequence<sup>2</sup> which  
65 is recognized by tailoring enzymes *via* a specific domain called RRE (RiPP precursor peptide  
66 recognition element)<sup>10</sup>. After modification, the leader sequence is cleaved off and the modified  
67 peptide secreted. If the general principles are well established, how post-translational  
68 modifications are installed and precursor peptides recognized by biosynthetic machineries  
69 remains largely elusive<sup>1,2</sup>.

70 Among the broad diversity of RiPP post-translational modifications, epimerization has been  
71 only marginally investigated. In eukaryotes, the L-to-D conversion of peptide residues is critical  
72 for the activity of various toxins, venoms and neuro-peptides<sup>11</sup>. However, the catalytic  
73 processes underpinning these transformations are largely unknown. In prokaryotes, the  
74 combined action of a dehydratase and a reductase has been shown to result in the conversion  
75 of L-Ser and L-Thr into D-Ala and D- $\alpha$ -aminobutyrate, respectively<sup>12,13</sup>. However, not only this  
76 transformation is restricted to Ser and Thr residues but it leads to the modification of the nature  
77 and reactivity of the amino acid side-chain.

78 Recently, novel RiPP families including proteusins<sup>14</sup> and eipeptides<sup>9</sup> have been shown to  
79 contain D-amino acid residues formed by the direct and irreversible epimerization of L-  
80 residues<sup>2,9,14,15</sup>. *In vivo* and *in vitro* studies have demonstrated that eipeptides induce the  
81 expression of LiaRS, a two-component system that orchestrates the cell envelope stress  
82 response in *Bacillus subtilis*<sup>16-18</sup>. This system, highly conserved among Firmicutes, regulates  
83 the expression of various genes involved in oxidative stress and cell wall antibiotic responses<sup>17-</sup>  
84 <sup>19</sup>. We have shown that the activity of eipeptides is strictly dependent on the presence of  
85 epimerized residues<sup>9</sup> (**Figs. 1a, b**) and established that they have a distinct mode of action  
86 compared to other known antimicrobial peptides<sup>18</sup>. In addition, we have demonstrated that  
87 eipeptides are widely distributed in the human microbiota<sup>9,17,18</sup> and that epimerizations are  
88 catalyzed by a radical S-adenosyl-L-methionine (SAM or AdoMet) enzyme called EpeE<sup>9,17</sup>.  
89 Radical SAM enzymes are central biocatalysts in RiPPs biosynthesis and have been shown  
90 to install an outstanding diversity of post-translational modifications<sup>4,5,8,20-26</sup>. However, until  
91 now, no radical SAM enzyme has been crystallized in complex with its peptide substrate  
92 properly positioned in the active site, limiting our understanding of their catalysis.

93 To decipher how radical SAM enzymes introduce post-translational modifications in RiPPs and  
94 catalyze epimerization, we have performed EPR, SEC-SAXS and structural analysis of the  
95 radical SAM epimerase EpeE from *B. subtilis*<sup>9,17</sup>. We circumvented the intrinsic difficulty to  
96 obtain RiPP-enzyme complexes by developing a RiPP-fragment based approach combined  
97 with targeted mutagenesis. This novel approach allowed to get at a high resolution, the first  
98 crystal structure of a RiPP-modifying radical SAM enzyme in interaction with its substrate. We  
99 have also solved the structure of several EpeE mutants and trapped an unexpected adduct on  
100 a reactive cysteine residue. Collectively, our work provides a structural and mechanistic  
101 rationale for peptide epimerization, a rare case of redox-neutral reaction catalyzed by radical  
102 SAM enzymes.

103

## 104 Results

### 105 EpeE, a RiPP radical SAM enzyme with a truncated TIM barrel

106 We crystallized EpeE anoxically in the presence of the S-adenosyl-L-methionine (SAM) or S-  
107 adenosylhomocysteine (SAH) cofactor. No significant structural difference was measured  
108 (r.m.s.d value of 0.293 Å) however, in subsequent experiments SAH gave high-resolution  
109 structures when co-crystallization was performed with peptide substrates. The structure of  
110 EpeE with SAH, featuring a homodimer in the asymmetric unit, was determined at resolution  
111 of 2.4 Å (**Fig. 1c**). Out of the 319 protein residues, electron density was observed for residues  
112 1 to 317 in both chains. EpeE exhibits several unique features: first, it is built on a truncated  
113 radical SAM domain consisting of an N-terminal partial triose-phosphate isomerase (TIM)  
114 barrel fold (*i.e.*  $\beta 6/\alpha 5$ ) instead of the canonical  $(\beta/\alpha) 6$  TIM barrel. Only the radical SAM  
115 enzymes QueE<sup>27</sup> and BtrN<sup>28</sup>, which modify small organic substrates, exhibit a shorter core  
116 domain (*i.e.* a  $\beta 6/\alpha 3$  and  $\beta 5/\alpha 4$  partial TIM barrel, respectively). Second, EpeE is devoid of the  
117  $\alpha 4a$  helix connecting  $\beta 4$ -sheet to  $\alpha 4$ -helix and found in all structurally characterized RiPP-  
118 modifying radical SAM enzymes<sup>29,30</sup> (**Extended Data Fig. 1a**). Among the radical SAM motifs,  
119 we identified the three cysteine residues (C14, C18 and C21) as coordinating the radical SAM  
120 [4Fe-4S] cluster with SAH bound, as expected, to the unique iron-atom through its carboxy  
121 and amino groups (**Fig. 1d**). The SAH ligand was further stabilized by the conserved GGE,  
122 ribose, "GXIXGXXE" and  $\beta 6$  motifs (**Extended Data Fig. 1b**)<sup>31</sup>. However, in the CX<sub>3</sub>CX $\Phi$ C  
123 motif, the  $\Phi$  residue is not an aromatic residue but H20 which coordinates both N6 and N7  
124 from the adenine moiety and unexpectedly stabilizes the ribose moiety *via* side-chain H-bond  
125 with O2' (**Extended Data Fig. 1b-c**). Finally, the GGE motif also contains a non-proline *Cis*-  
126 peptide bond between the two glycine residues.

### 127 A C-terminal domain with an unusual architecture

128 As a hallmark, radical SAM enzymes involved in peptide or protein post-translational  
129 modifications have been shown to possess a C-terminal domain housing additional iron-sulfur  
130 clusters. This C-terminal domain is either between 106-115 residues long with two auxiliary  
131 iron-sulfur clusters and called a SPASM domain<sup>29,30,32,33</sup>, or significantly shorter and  
132 unstructured with a single iron-sulfur cluster and called a twitch domain<sup>34</sup>. Single anomalous  
133 diffraction at the peak absorption wavelength of iron was consistent with the presence of four  
134 iron-sulfur clusters in the EpeE dimer (**Extended Data Table 1**). Besides the radical SAM [4Fe-  
135 4S] cluster, a single auxiliary cluster (AuxI), best accounted for by a [4Fe-4S] cluster and fully  
136 ligated by four cysteine residues (C206, C222, C289 and C292) was identified (**Fig. 1d**). Two  
137 of these 4 cysteine ligands are flanking the conserved  $\beta$ -hairpin while the other two are  
138 localized in the  $\alpha 4'$  helix. This iron-sulfur cluster, located at 16.9 Å from the radical SAM cluster,  
139 belongs to the C-terminal domain which overall length (111 residues) unexpectedly exceeds  
140 the size of a twitch domain. In addition, the  $\beta 6$ - $\beta 1'$  bridging loop makes extensive H-bond  
141 interactions with the  $\alpha 3'$  helix and the  $\alpha 3'$ - $\alpha 4'$  loop and extends toward the location where the  
142 second cluster is found in SPASM domains (**Extended Data Fig. 2**)<sup>35</sup>. Additional helices ( $\alpha 3'$ ,  
143  $\alpha 4'$ ,  $\alpha 5'$ ), absent in twitch domains and involving a tight H-bond network,  $\pi$ - $\pi$  stacking and  
144 hydrophobic interactions, are also present establishing a unique and high secondary structure  
145 organization (**Extended Data Fig. 1a, 2**). Overall, the EpeE structure blurs the demarcation  
146 between SPASM and twitch domains and defines a transient architecture that we propose to  
147 call a T-SPASM domain.

148

### 149 EPR spectroscopic characterization of EpeE

150 To investigate the properties of the two iron-sulfur clusters, we analyzed EpeE by EPR  
151 spectroscopy. The EPR spectrum of EpeE, after reconstitution and reduction, showed a single  
152 paramagnetic component characterized by an axial shape with  $g$ -values  $g_{\parallel} = 2.036$  and  $g_{\perp} =$   
153  $1.929$ , which are typical for a reduced  $S = \frac{1}{2}$  radical SAM  $[4\text{Fe-4S}]^+$  cluster (**Fig. 1e**, trace 1)<sup>36</sup>.  
154 The signal displayed significant relaxation broadening at temperatures above 30 K when  
155 recorded under non-saturating microwave power (**Extended Data Fig. 3a, b**). Consistent with  
156 this assignment, it disappeared in the A3-mutant, in which the three cysteines coordinating the  
157 radical SAM cluster have been substituted by alanines (**Fig. 1e**, trace 3). Iron-sulfur  
158 determination indicated that, in agreement with its UV-visible spectrum, the reconstituted wild-  
159 type EpeE contained  $8.6 \pm 0.5$  mol of Fe per mole of protein whereas the A3-mutant contained  
160  $4.8 \text{ mol} \pm 0.13$  of Fe per mole of protein (**Extended Data Fig. 3c**). This supports the presence  
161 of two and one  $[4\text{Fe-4S}]$  cluster in the wild-type and A3-mutant, respectively. Therefore, the  
162 absence of any other signal in the reduced wild-type or A3-mutant is consistent with the fact  
163 that the auxiliary cluster is in the EPR silent  $[4\text{Fe-4S}]^{2+}$  redox state, most probably because of  
164 its very low redox potential as reported for other radical SAM enzymes<sup>37,38</sup>. The addition of  
165 SAM to the dithionite-reduced wild-type enzyme induced a substantial change in the  
166 resonance position and shape of the EPR spectrum. Notably, a signal from an  $S = \frac{1}{2}$   
167 paramagnetic species having all  $g$ -values smaller than 2.00 (*i.e.*  $g_{1,2,3} = (1.983, 1.871, 1.790)$ )  
168 was detected, as shown in the spectrum measured at 6 K under non-saturating conditions  
169 (**Fig. 1e**, trace 4 & **Extended Data Fig. 3a, b**). Absent from the A3-mutant (**Fig. 1e**, trace 6),  
170 this signal is assigned to a SAM-bound form of the radical SAM  $[4\text{Fe-4S}]^+$  cluster. Radical SAM  
171  $[4\text{Fe-4S}]^+$  clusters having all  $g$ -values smaller than 2.0 have been reported for other  
172 enzymes<sup>33,39,40</sup> and generally associated with a cluster form in which SAM binds to the unique  
173 iron of cluster, an assignment further supported by HYSCORE measurements (**Extended Data**  
174 **Fig. 3d**).

### 175 **Structure of EpeE in complex with a peptide substrate**

176 Initial attempts to crystallize EpeE with its full-length substrate failed, as commonly  
177 encountered with RiPP-modifying enzymes. This recurrent failure likely results because of the  
178 intrinsically disordered nature of peptides and the fact that many RiPP-modifying enzymes  
179 have relaxed substrate specificity, essential to introduce post-translational modifications at  
180 distinct sites<sup>41</sup>. Indeed, EpeE like other radical SAM enzymes<sup>15,42</sup> introduces multiple post-  
181 translational modifications and must thus adapt to different peptide contexts. To circumvent  
182 this inherent difficulty, we designed a peptide library covering the leader and core sequence of  
183 the peptide substrate EpeX 1 (**Fig. 2a**). This RiPP-fragment library was assayed for activity  
184 and co-crystallization with EpeE. All peptides containing the core sequence (peptides 4-7)  
185 proved to be substrates as shown by labeling experiments performed in deuterated buffer  
186 (**Extended Data Fig. 4, 5 and Supplementary Tables 1-8**)<sup>9,15,43</sup>. LC-MS/MS analysis notably  
187 confirmed that <sup>2</sup>H-atom incorporation occurred exclusively at the expected epimerization sites.  
188 Of note, with peptides 4 and 7, we monitored significant uncoupling between SAM cleavage  
189 and epimerization activity, as revealed by 5'-dA isotopic enrichment (**Extended Data Fig. 4a,**  
190 **d**). In contrast, with peptides 5 and 6, no solvent <sup>2</sup>H-atom was incorporated into 5'-dA,  
191 supporting a strict coupling with these substrates (**Extended Data Fig. 4b, c & Extended Data**  
192 **Fig. 5**).

193 Remarkably, EpeE co-crystallization assays under anaerobic conditions with SAH and the  
194 RiPP-fragment library, led to a high-resolution structure (2.39 Å) of EpeE in complex with  
195 peptide 5 (**Fig. 2a & b**). Crystal form in space group  $P2_12_12_1$  was identical to the one obtained

196 when crystallizing the substrate-free enzyme, with an asymmetric unit consisting of a  
197 homodimer (**Extended Data Table 1**). Only subtle changes mainly located in the T-SPASM  
198 domain could be measured between the free- and bound-substrate structures (r.m.s.d of 0.78  
199 Å, **Extended Data Fig. 6**). In addition, a strong electron density for the peptide **5** was observed  
200 for 7 out of 11 residues (**Extended Data Fig. 7a**). The peptide fits in the open cavity located  
201 at the bottom of the partial TIM barrel and binds between the  $\beta$ 1- $\beta$ 5 of the radical SAM domain  
202 and the beginning of the T-SPASM domain (**Fig. 2b**). Peptide **5** is coordinated by a complex  
203 network of inter- and intra-molecular interactions folding partially the peptide into a  $3_{10}$ -helix  
204 (**Extended Data Fig. 7b**). The residue target of the modification I44 is in the vicinity (3.6 Å) of  
205 the aromatic rings of F23 and F228 (**Fig. 2c**). Interestingly C223, which we proposed as the  
206 H-atom donor of the reaction<sup>9</sup>, is part of the hydrophobic pocket around I44 and provides key  
207 interactions with I44 including a polar contact *via* its backbone oxygen and hydrophobic  
208 interactions. I44 is also stabilized through its backbone oxygen by hydrogen bonding with the  
209 sidechain oxygen of T57 (**Fig. 2c**). Further stabilization of the substrate is provided by  $\pi$ - $\pi$   
210 stacking between W43 and the aromatic ring of F175 (EpeE) ( $\pi$ - $\pi$  centroids 4.6-5.4 Å). Finally,  
211 polar interactions with the adenine moiety of SAH (3.28 Å) and hydrophobic contacts with I178  
212 and P225 (3.59 Å) are also involved in stabilizing I44 through W43 (**Fig. 2c**). The importance  
213 of W43 in peptide stabilization is consistent with the fact that the two epimerization sites (I44  
214 and V36), despite lacking sequence homology, are preceded by an aromatic residue. Hence,  
215 EpeE appears to recognize a hydrophobic motif for epimerization installation. Further  
216 interactions between EpeE and its substrate involve salt bridges between the sidechain of  
217 D210 and the sidechains of two substrates residues, R42 and N41, this latter having also a  
218 direct interaction with G208 (**Fig. 2c**). The radical SAM domain through S55 and T57 side  
219 chains also contributes to peptide stabilization mainly through polar contacts, while T113 and  
220 L84 interact with L45 from the peptide through water contacts. Similarly, N147 ( $\beta$ 5) coordinates  
221 a water molecule that makes polar contacts with three residues (T43, L45 and R42) from  
222 peptide **5** (**Fig. 2c**). Hence, the structure of the complex revealed that the substrate not only  
223 interacts with the two protein domains but also with the SAH cofactor. It also surprisingly  
224 showed that the substrate residues preceding I44 adopt a  $3_{10}$ -helix secondary structure.

225

### 226 **Cys223 as a critical H-atom donor**

227 In the enzyme-substrate complex, the distance between the targeted substrate residue I44 C $_{\alpha}$ -  
228 atom and the C5'-atom of SAM (3.8 Å) is perfectly suited for direct H-atom abstraction from  
229 the substrate. Remarkably, on the opposite side of I44, we found C223 (S<sub>C223</sub>-C $_{\alpha}$ -I44-C5'<sub>SAH</sub>  
230 angle: 152°) with a sulfur (C223) to C $_{\alpha}$ -atom (I44) distance of 6.3 Å (**Fig. 2d**). Although this  
231 distance is too large for direct interaction between C223 and the transient peptide carbon-  
232 centered radical formed during catalysis, this distance is likely to shorten due to the loss of I44  
233 stereochemistry. In addition, the structure of the D210A mutant (see below) has revealed that  
234 C223 can sample other conformations bringing the sulfhydryl group 2 Å closer to the radical  
235 SAM [4Fe-4S] cluster. Altogether, these data are in full agreement with the proposed role of  
236 C223 as the H-atom donor of the reaction.

237

### 238 **Crystallographic snapshots of an EpeE active-site mutant**

239 Because of the critical role of C223 in the epimerization reaction, we reasoned that the C223A  
240 mutant could provide further stabilization to the transient peptide-protein complex. Structure of  
241 this mutant perfectly superimposed with the one of the wild-type enzyme (r.m.s.d. value of  
242 0.2945 Å,) with the SAM cofactor in direct interaction with the radical SAM [4Fe-4S] cluster.

243 EPR analysis of this mutant (**Fig. 1e**, traces 2 & 5), in the absence or the presence of SAM,  
244 showed identical EPR signatures than the wild-type EpeE, supporting that the electronic  
245 structure of the radical SAM [4Fe-4S]<sup>+</sup> cluster is not affected.

246 Gratifyingly, we solved the structure of the C223A mutant at an atomic resolution with peptide  
247 **5** and peptide **6** (1.75 Å and 2.15 Å, respectively) in the presence of SAH. Interactions between  
248 peptide **5** and the C223A mutant were overall similar to the wild-type enzyme (r.m.s.d 0.22 Å)  
249 (**Figs. 3a and Extended Data Fig. 8**). However, we obtained electron density for two additional  
250 *N*-terminal amino acid residues located at the very entrance of the active site and forming an  
251 additional turn, pointing toward the exit of the active site (**Fig. 3a and Extended Data Fig. 8c**).

252 The peptide **6**-C223A mutant complex revealed the structure of the full *C*-terminal end of EpeX  
253 **1** (**Fig. 3b and Extended Data Fig. 8c**). This final peptide segment is stabilized along three β-  
254 sheets from the partial TIM barrel (from β3 to β5) and points toward the exit of the active site  
255 with the final peptide residue H49 making polar contacts with I144, S145 and D143.  
256 Interestingly, D143 and K171 from EpeE are stacking H49 (**Fig. 3b**), while in the complex with  
257 peptide **5** (lacking H49) and in the substrate-free structure, D143 and K171 are stabilized by a  
258 salt bridge in a distinct orientation (**Extended Data Fig. 8d, e**).

259 The overlapping sequences of peptides **5** and **6** perfectly superimposed, demonstrating the  
260 validity of our RiPP-fragment based approach (**Fig. 3c**). Notably, in both complexes, the  
261 relative location of I44 within the active site, remains the same. Unexpectedly, the presence of  
262 H49 provides further inter-chain interactions between the two enzyme subunits (**Extended**  
263 **Data Fig. 8d, e**). Within the homo-dimeric complex, peptide-peptide interactions are thus likely  
264 to significantly contribute to stabilize a productive positioning of the substrate. Exploiting these  
265 two atomic-resolution structures, we were able to model, based on the visible electron density,  
266 the structure of a peptide spanning 13 residues long (**Fig. 3d**). In this model, I44 is part of a  
267 folded peptide region as a 3<sub>10</sub>-helix while the final GSGH motif has an extended conformation.  
268 Remarkably, hydrophobic side-chains are protruding (I44, W43) and alternating with charged  
269 residues (E40, R42), reminiscent of the structure of α-helical antimicrobial peptides<sup>44</sup>.

270

### 271 **Structural basis for RiPP epimerization**

272 As shown, in all the peptide-enzyme complexes obtained, I44 is perfectly positioned for C $\alpha$  H-  
273 atom abstraction (**Fig. 4a**) and formation of a carbon-centered radical. This transient reaction  
274 intermediate is likely to react with the sulfhydryl of C223, leading to epimerization of I44 and  
275 the formation of a thiyl radical. With the auxiliary cluster (AuxI) in the vicinity of C223, a  
276 consistent function would be as an electron shuttle to the thiyl radical. Only few radical SAM  
277 RiPP-modifying enzymes have been spectroscopically characterized<sup>37,45,46</sup> but for some of  
278 them, the auxiliary cluster (AuxI) proved to be a low-potential [4Fe-4S] cluster<sup>37</sup>. In addition,  
279 recent investigations have shown that substrate binding can tune the redox properties of the  
280 AuxI cluster, further supporting a role as an electron shuttle<sup>46</sup>. In EpeE, AuxI is likely to fulfill a  
281 similar function with two tyrosine residues (Y209 and Y2) located beneath the cluster and  
282 stabilized by main chain interactions, hydrogen bonds and π-π stacking, ideally positioned to  
283 serve as an electron conduit from the protein surface (**Fig. 4a**). In addition, we also identified  
284 in the immediate environment of C223, only one titratable residue: D210. This residue provides  
285 key electrostatic interactions to the substrate (**Figs. 2c, 3a and 3b**) and is stabilized by a polar  
286 bond with T5 (**Extended Data Fig. 9a**).

287 To probe for the function of these residues, we generated several mutants by substituting the  
288 two tyrosines with phenylalanine residues (Y2F-Y209F mutant) and by replacing D210 with an

alanine residue (D210A mutant). The activity of these mutants was assayed using peptide **6** as substrate and a physiological reducing system (NADPH/flavodoxin/flavodoxin reductase). As shown, we obtained a tight coupling between SAM cleavage (5'-dA production) and peptide epimerization with the wild-type enzyme (**Fig. 4b**). In contrast, with the C223A mutant, epimerization was strongly impaired while SAM cleavage activity remained similar to the wild-type enzyme. Hence, with the C223A mutant, only the epimerization reaction is affected. The two other mutants Y2F-Y209F and D210A had similar activities compared to the wild-type EpeE (**Fig. 4b**). However, under *in vitro* conditions, the physiological roles of these amino acid residues might be difficult to evidence because of the excess of reductant and electrons present in the reaction mixtures.

The high-resolution structure of the D210A mutant in complex with SAH (1.95 Å) was similar to the wild-type enzyme (r.m.s.d. of 0.25 Å). However, it exhibited two major differences: first, C223 adopted a distinct orientation bringing the sulfhydryl group 2 Å closer toward the SAH cofactor. Second, we noted the presence on C223 of an additional electron density (**Extended Data Fig. 9b**). This extra electron density was modeled, after analysis of the  $2F_o - F_c$  map maximum intensity, as a second sulfhydryl group (**Extended Data Fig. 9b**). The presence of a persulfur on a reactive cysteine has been reported in several systems including cytochrome thiosulfate dehydrogenase<sup>47</sup> or the cysteine desulfurase NifS<sup>48</sup>. In the D210A mutant, the origin of this additional sulfur atom is unknown but it supports that C223 is a reactive residue. Careful analysis of all structures showed that this adduct and this sidechain orientation were only present in the D210A mutant, supporting that D210 plays an important role to stabilize C223. Finally, polar contacts between D210 and T5 sidechains are also reminiscent of the catalytic “acid-alcohol pair” found in cytochrome P450<sup>49</sup> and involved in proton transfer within the active site. Collectively, these data support that D210 interacts with C223 and could play an important role not only in substrate stabilization and positioning, but also for C223 reactivity.

314

## 315 Discussion

Despite major advances in our understanding of RiPP biosynthesis, core peptide recognition by RiPP enzyme active sites is largely unknown. These enzymes must often recognize multiple modification sites to generate their final products, supporting a relaxed substrate specificity. Recent studies have shown that RiPP-modifying enzymes including radical SAM enzymes, while catalyzing a vast array of chemical transformations<sup>1,2</sup>, share conserved structural features such as an RRE to interact with the leader peptide<sup>10</sup> and ensure the fidelity of the post-translational modifications. However, this structural element is absent from many enzymes questioning the processes underpinning their specificity.

To address these fundamental questions, we have investigated the radical SAM epimerase EpeE<sup>9</sup> alone and in complex with several peptide substrates. Structural and EPR analyses demonstrate that EpeE contains two [4Fe-4S] clusters and has an unusual architecture. Its compact fold markedly differs from all known RiPP-modifying radical SAM enzymes by the notable absence of an RRE domain and of the  $\alpha_6$  and  $\alpha_{4a}$  helices from the partial TIM barrel. In addition, EpeE possesses a unique C-terminal domain which shares the single [4Fe-4S] cluster of twitch-domains but with an overall fold reminiscent of the SPASM-domain, that we propose to call a T-SPASM domain (**Figs. 1 & 2**).

By generating a RiPP-fragment library, we were able to obtain high-resolution crystallographic snapshots of a RiPP-modifying radical SAM enzyme in a pre-catalytic state (**Figs. 2b, c and**

334 **Extended Data Fig. 8**) with its substrate properly located in the active site. Currently, only two  
335 structures of radical SAM enzymes catalyzing RiPP post-translational modifications have been  
336 solved in complex with peptide substrates<sup>29,30</sup>. Intriguingly, in SuiB, which catalyzes the  
337 formation of carbon-carbon bonds, the leader peptide was found in the partial TIM barrel  
338 instead of the RRE and no electron density was present for the core peptide. For CteB which  
339 catalyzes thioether bond formation, only the leader peptide sequence and the first three  
340 residues of the core region were visible in the co-crystallized structure<sup>30</sup>.

341 In sharp contrast, the structures of EpeE and its C223A mutant in complex with different  
342 peptide substrates revealed that I44, the amino acid residue target of the modification, is in an  
343 ideal position for direct C<sub>α</sub> H-atom abstraction by the 5'-dA radical (I44 C<sub>α</sub>-atom-C5' distance  
344 of 3.8 Å). Structural analysis also revealed that a conserved cysteine residue (C223) is located  
345 beneath I44 to serve as an H-atom donor. By using a physiological reductant system, we  
346 demonstrated that while the SAM cleavage activity is not affected by mutation of C223, the  
347 second part of the reaction (*i.e.* H-atom transfer to the carbon-centered radical) is hampered  
348 leading to a strong uncoupling between SAM cleavage and peptide epimerization (**Fig. 4b**).  
349 Interestingly, while the distance in the peptide-enzyme complex is too long (6.3 Å, **Fig. 2d**) for  
350 a direct interaction between C223 and the C<sub>α</sub>-atom of I44, structural analysis of the D210A  
351 mutant revealed that C223 can sample various conformations, bringing the sulfur atom closer  
352 to the I44 C<sub>α</sub>-atom. Altogether, these results support that radical SAM peptide epimerases  
353 effectively use a cysteine residue as critical H-atom donor, a strategy likely common to all  
354 radical SAM epimerases<sup>15,50,51</sup>.

355 Another advantage of our RiPP-fragment based approach was to gain structural information  
356 regarding RiPP structure during catalysis. Indeed, based on the structure of several peptide-  
357 enzyme complexes, we were able to model up to 13 substrate residues, starting from the  
358 residue after V36 up to the C-terminal end of EpeX. This model reveals that EpeX is partially  
359 folded as a 3<sub>10</sub>-helix in the enzyme active site with protruding hydrophobic side-chains.  
360 Although 3<sub>10</sub>-helices have been identified in other RiPPs, the core region is usually  
361 unstructured or with a U-turn shape in RiPP-enzyme complexes<sup>52-55</sup>.

362 In sharp contrast to the known structures of (non-radical SAM) RiPP-modifying enzymes<sup>52-55</sup>,  
363 only minor rearrangements occurred in EpeE upon substrate binding. Peptide-enzyme  
364 interactions are driven not only by residues from the radical SAM domain but also by residues  
365 from the T-SPASM domain and the SAM cofactor itself, forging a complex network of  
366 interactions that ensure substrate recognition in the absence of RRE. Interestingly, a similar  
367 strategy implying interactions between the substrate backbone with the protein domains and  
368 the SAM cofactor, has been recently reported for the B<sub>12</sub>-dependent radical SAM enzyme  
369 Mmp10<sup>56</sup>.

370 Another intriguing finding of this study is that with peptide **6**, not only the full C-terminal end of  
371 eptideptide could be accommodated in the EpeE dimer without steric clashes but unexpectedly,  
372 further stabilization was provided by the last residue. Indeed, H49, stacked between K171 and  
373 D143, directly interacts through inter-chain interactions with H49 from the second subunit  
374 (**Extended Data Fig. 8d, e**), supporting a physiological role for the dimer (**Fig. 5a**). To validate  
375 this model, we performed anaerobic SEC-SAXS analysis in order to determine the  
376 oligomerization state of EpeE in solution. SEC-SAXS analysis showed that anaerobically  
377 reconstituted EpeE in the presence of SAM behaved as a homogenous globular and folded  
378 protein (**Fig. 5b**) with a radius of gyration of 28.7 Å and an estimated molecular weight of 73-  
379 71 kDa. These experimental data are consistent with EpeE being exclusively a dimer in

380 solution and are in full agreement with our structural analysis. Additionally, surface interaction  
381 calculations using the PDBePISA server<sup>57</sup> also supported that the dimer is the most stable  
382 species (**Supplementary Tables 9-10**). This dimer provides an elegant structural rationale for  
383 the installation of the two epimerizations in epeptides. Initially, two peptide molecules interact  
384 within the EpeE dimer, positioning I44 in the active site for direct attack by the 5'-dA radical.  
385 The presence of a hydrophobic residue before each targeted residue is also likely to provide  
386 key stabilization. Following H-atom abstraction, the amino acid configuration is lost (**Fig. 5c**)  
387 and the radical substrate intermediate is quenched by C223, which is ideally located on the  
388 opposite side of the targeted residue. Similar critical cysteine residues have been identified in  
389 all radical SAM epimerases investigated to date<sup>15,50,51</sup>. After configuration inversion, a transient  
390 thiyl radical is generated on C223. D210 which forms a pair with T5 and stabilizes C223, is the  
391 only residue that could serve to regenerate the thiyl radical using a proton-coupled electron  
392 transfer pathway. Following, the first epimerization event, the dimer progresses toward V36  
393 which is already in the vicinity the active site (**Fig. 5a**). In support of this model, not only we  
394 have always crystallized peptides with I44 positioned for H-atom abstraction but also I44 was  
395 always the hotspot for epimerization (**Extended Data Fig. 4**), suggesting a *C-to-N* directionality  
396 in EpeE like in PoyD<sup>15</sup>.

397 In conclusion, our study reports an unprecedented binding mode for a RiPP-modifying enzyme  
398 and expands the structural diversity of radical SAM enzymes catalyzing RiPP post-translational  
399 modifications. Unexpectedly, the EpeE structure reveals that inter-chain interactions could play  
400 a significant role for the sequential installation of epimerizations. Finally, this work illuminates  
401 how radical SAM enzymes catalyze peptide epimerization, a rare example of redox-neutral  
402 reaction, delineating novel reactivity in enzyme active sites.



403 **Acknowledgments**

404 This work was supported by the French National Research Agency (ANR grants: ANR-17-  
405 CE11-0014 to O.B.; ANR-20-CE44-0005 to O.B.). The authors are grateful to the EPR facilities  
406 available at the French EPR network (IR CNRS 3443, now INFRANALYTICS, FR2054) and  
407 the Aix-Marseille University EPR center. We acknowledge SOLEIL (Saint-Aubin, France) for  
408 provision of synchrotron radiation facilities and we would like to thank the PROXIMA-1 and  
409 SWING staff for assistance in using the beamline.

410

411 **Author contributions**

412 A.B. & O.B. research design and funding acquisition; X.K., I.P., L.M.G.C., C.D.F., A.G., S.G.,  
413 G.G., .A.T., P.L., O.B. & A.B performed research; X.K., I.P., L.F. & C.B. protein production.  
414 X.K., I.P., L.M.G.C., C.D.F., A.G., S.G., G.G., .A.T., P.L., O.B. & A.B. analyzed data. O.B. &  
415 A.B. wrote the manuscript with contributions from co-authors.

416

417 **Competing Interests Statement**

418 The authors declare no competing interests.

419

420 **Additional information**

421 Extended data is available for this paper.

422

423

424

425

## Figure legends

426  
427  
428  
429  
430  
431  
432  
433  
434  
435  
436  
437  
438  
439  
440  
441  
442  
443  
444  
445

**Fig. 1 - Epipeptide biosynthesis and overall structure of the EpeE radical SAM epimerase.** **a**, Sequence of EpeX precursor with the leader (white circles) and the core peptide sequence (blue circles) indicated. After modification by EpeE, the mature epipeptide is produced with epimerization of V36 and I44 (in red). **b**, Epimerization reaction catalyzed by EpeE showing the C $\alpha$  H-atom, target of the modification, in red. **c**, Overall structure of the EpeE homodimer in the asymmetric unit (left panel). Radical SAM domain (light blue, residues 1-175) and T-SPASM domain coordinating the auxiliary (AuxI) [4Fe-4S] cluster (teal, residues 206-317). **d**, Crystal structure of EpeE with bound SAH. The [4Fe-4S] and AuxI clusters are shown as balls and sticks (yellow and orange spheres) and SAH as sticks (green). The omit map (blue mesh) of SAH and [4Fe-4S] clusters are contoured at 3 $\sigma$ . AuxI: auxiliary cluster. **e**, EPR analysis of EpeE. X-band CW EPR spectra of dithionite-reduced reconstituted samples of EpeE WT (traces 1, 4), C223A mutant (traces 2, 5) and **A3**-mutant (traces 3, 6) and in the absence (traces 1-3) and presence (traces 4-6) of an excess of SAM. Experimental conditions: temperature, 15 K (traces 1-3) or 6 K (trace 4-6), microwave power, 0.1 mW, field modulation amplitude, 1 mT, microwave frequency, 9.48 GHz, number of accumulations, 8 (1-3), or 16 (4-6). Protein concentration, 320  $\mu$ M (1, 4), 223  $\mu$ M (2, 5), 380  $\mu$ M (3, 6), SAM concentration, 1 mM.

446  
447  
448  
449  
450  
451  
452  
453  
454  
455  
456  
457  
458  
459  
460  
461  
462  
463  
464  
465

**Fig. 2 - Structure of EpeE in interaction with a peptide substrate and SAH cofactor.** **a**, Sequences of the peptide substrates assayed: EpeX (peptide **1**) and the RiPP-fragments: peptides **2**, **3**, **4**, **5**, **6** & **7**. The leader peptide is shown in white circles and the core peptide is indicated by blue circles. The two residues, targets of the modification by EpeE (*i.e.* V36 and I44) are shown in red in blue circles. **b**, Overall structure of EpeE in complex with the peptide **5** (left panel). The bound peptide **5** (residues K<sub>39</sub>ENRWIL<sub>45</sub>) is depicted in pink sticks, SAH is shown in green and the two [4Fe-4S] clusters are in yellow and orange. APBS-derived surface electrostatics of EpeE reveals three distinct electrostatic potentials in the EpeE peptide binding pocket (right panel). Surface colored according to electrostatic potential with positively charged regions in blue and negatively charged regions in red. The bound peptide is shown in pink sticks. **c**, Coordination of the peptide **5** (pink sticks) by both EpeE domains. The binding pocket within 5 Å of the peptide consists of 6 hydrophobic residues (F23, F175, F228, L84, I85, I178), five polar uncharged residues (S55, T57, T83, T113, S224), and three charged residues (N9, N147, D210), in addition to C223, P176 and P225. SAH, the radical SAM [4Fe-4S] and AuxI clusters are shown as sticks. Amino acid residues in light blue belong to the radical SAM domain and the ones in teal are from the T-SPASM domain. **d**, Close-up of the EpeE active site showing SAH in green, the peptide **5** in pink, C223 in teal and the two [4Fe-4S] clusters in yellow and orange. The distances between the C5' atom of SAH and the C $\alpha$  atom of I44 from peptide **5** (3.8 Å) and between I44 and the sulfur-atom of C223 from EpeE (6.3 Å) are indicated by dashed lines.

466

467  
468  
469  
470  
471  
472  
473

**Fig. 3 - Structures of C223A mutant in interaction with two peptide substrates and SAH cofactor.** **a**, Close-up of EpeE **C223A** mutant active site showing protein residues from the radical SAM (in light blue) and the T-SPASM (in teal) domains in interaction with the peptide **5** (in pink). Dashed lines show polar contacts between peptide **5** and protein residues. SAH is depicted in green sticks and both [4Fe-4S] clusters are shown in yellow and orange spheres. **b**, Close-up of EpeE **C223A** mutant active site showing protein residues from the radical SAM (in light blue) and the T-SPASM (in teal) domains in interactions with the peptide **6** (in light

474 green). Dashed lines show polar contacts between peptide **6** and protein residues. SAH is  
475 depicted in green sticks and both [4Fe-4S] clusters in yellow and orange spheres. The  
476 epeptide C-terminal region points toward the exit of the active site with the last residue H49  
477 interacting with residues 143-145. **c**, Superimposition of the structures of peptides **5** and **6**  
478 obtained from the respective complexes with the **C223A** EpeE mutant. **d**, Model of the 13  
479 residues (KSKENRWILGSGH) identified in C223A EpeE mutant active site. The region that  
480 holds I44 is folded as a  $3_{10}$ -helix while the C-terminal residues (GSGH) featured an extended  
481 conformation.

482

483 **Fig. 4 – Amino acid network in the active site of the radical SAM enzyme EpeE.** **a**, Close-  
484 up of EpeE active site with key residues highlighted. Distances are shown as dotted lines with  
485 values indicated in Å. **b**, Time-course analysis of epimerized peptide (open and closed  
486 squares) and 5'-dA (open and closed diamonds) production by EpeE and mutants (**C223A**,  
487 **D210A** & **Y2F/Y209F**) incubated with SAM and peptide **6** under anaerobic and reducing  
488 conditions with the flavodoxin/flavodoxin reductase/NADPH system. Experiments were  
489 performed in duplicate and analyzed by LC-MS.

490

491 **Fig. 5 – Substrate interaction and proposed mechanism for EpeE.** **a**, Model of  
492 epimerization catalyzed by EpeE on the EpeX peptide. In the EpeE dimer, two peptide  
493 molecules (EpeX) interact through inter- (H49) and intra-chain interactions with I44 positioned  
494 in the active site for an attack by the 5'-dA radical. After the first epimerization event, the dimer  
495 progresses toward V36, the second epimerized residue. **b**, SEC-SAXS analysis of EpeE in the  
496 presence of SAM (panel 1) or SAM and peptide **6** (panel 2). The UV visible signal at  $\lambda = 280$   
497 nm (blue) and SAXS intensity at zero angle (red) is superimposed with the computed Rg from  
498 SAXS data (open circles). SAXS curves of EpeE in the presence of SAM (panel 3) and EpeE  
499 in the presence of SAM and peptide **6** (panel 4). Fit curves using PepsiSAXS are indicated by  
500 a red trace and  $\chi^2$  value determined between the experimental data and the simulated model  
501 (see **Supplementary Table 10**). **c**, Proposed mechanism for EpeE. Following the reduction of  
502 the radical SAM cluster, the 5'-dA radical generated, abstracts the C $_{\alpha}$  H-atom of the target  
503 residue. The carbon-centered radical formed on the substrate reacts with C223, leading to  
504 configuration inversion of I44 and formation of a thiyl radical on C223. The AuxI [4Fe-4S]  
505 cluster, likely assisted by D210, is ideally positioned to regenerate C223 through a proton-  
506 coupled electron transfer pathway.

## References

- 507  
508  
509 1. Montalban-Lopez, M. et al. New developments in RiPP discovery, enzymology and  
510 engineering. *Nat Prod Rep* **38**, 130-239 (2021).  
511 2. Benjdia, A. & Berteau, O. Radical SAM Enzymes and Ribosomally-Synthesized and Post-  
512 translationally Modified Peptides: A Growing Importance in the Microbiomes. *Front Chem* **9**,  
513 678068 (2021).  
514 3. Benjdia, A. & Berteau, O. Sulfatases and radical SAM enzymes: emerging themes in  
515 glycosaminoglycan metabolism and the human microbiota. *Biochem. Soc. Trans.* **44**, 109-15  
516 (2016).  
517 4. Balty, C. et al. Ruminococcin C, an anti-clostridial sactipeptide produced by a prominent  
518 member of the human microbiota *Ruminococcus gnavus*. *J Biol Chem* (2019).  
519 5. Balty, C. et al. Biosynthesis of the sactipeptide Ruminococcin C by the human microbiome:  
520 Mechanistic insights into thioether bond formation by radical SAM enzymes. *J Biol Chem* **295**,  
521 16665-16677 (2020).  
522 6. Balskus, E.P. The Human Microbiome. *ACS Infect. Dis.* **4**, 1-2 (2018).  
523 7. Donia, M.S. et al. A systematic analysis of biosynthetic gene clusters in the human microbiome  
524 reveals a common family of antibiotics. *Cell* **158**, 1402-14 (2014).  
525 8. Benjdia, A., Balty, C. & Berteau, O. Radical SAM Enzymes in the Biosynthesis of Ribosomally  
526 Synthesized and Post-translationally Modified Peptides (RiPPs). *Front. Chem.* **5**, 87 (2017).  
527 9. Benjdia, A., Guillot, A., Ruffié, P., Leprince, J. & Berteau, O. Post-translational modification  
528 of ribosomally synthesized peptides by a radical SAM epimerase in *Bacillus subtilis*. *Nat Chem*  
529 **9**, 698-707 (2017).  
530 10. Burkhart, B.J., Hudson, G.A., Dunbar, K.L. & Mitchell, D.A. A prevalent peptide-binding  
531 domain guides ribosomal natural product biosynthesis. *Nat Chem Biol* **11**, 564-70 (2015).  
532 11. Heck, S.D. et al. Posttranslational amino acid epimerization: enzyme-catalyzed isomerization  
533 of amino acid residues in peptide chains. *Proc Natl Acad Sci U S A* **93**, 4036-9 (1996).  
534 12. Huo, L. & van der Donk, W.A. Discovery and Characterization of Bicereucin, an Unusual d-  
535 Amino Acid-Containing Mixed Two-Component Lantibiotic. *J Am Chem Soc* **138**, 5254-7  
536 (2016).  
537 13. Lohans, C.T., Li, J.L. & Vederas, J.C. Structure and biosynthesis of carnolysin, a homologue of  
538 enterococcal cytolysin with D-amino acids. *J Am Chem Soc* **136**, 13150-3 (2014).  
539 14. Freeman, M.F. et al. Metagenome mining reveals polytheonamides as posttranslationally  
540 modified ribosomal peptides. *Science* **338**, 387-90 (2012).  
541 15. Parent, A. et al. Mechanistic Investigations of PoyD, a Radical S-Adenosyl-L-methionine  
542 Enzyme Catalyzing Iterative and Directional Epimerizations in Polytheonamide A  
543 Biosynthesis. *J Am Chem Soc* **140**, 2469-2477 (2018).  
544 16. Butcher, B.G., Lin, Y.P. & Helmann, J.D. The yydFGHIJ operon of *Bacillus subtilis* encodes a  
545 peptide that induces the LiaRS two-component system. *J Bacteriol* **189**, 8616-25 (2007).  
546 17. Popp, P.F. et al. The Epipeptide Biosynthesis Locus epeXEPAB Is Widely Distributed in  
547 Firmicutes and Triggers Intrinsic Cell Envelope Stress. *Microb Physiol*, 1-12 (2021).  
548 18. Popp, P.F., Benjdia, A., Strahl, H., Berteau, O. & Mascher, T. The Epipeptide YydF Intrinsically  
549 Triggers the Cell Envelope Stress Response of *Bacillus subtilis* and Causes Severe Membrane  
550 Perturbations. *Front Microbiol* **11**, 151 (2020).  
551 19. Radeck, J. et al. Anatomy of the bacitracin resistance network in *Bacillus subtilis*. *Mol Microbiol*  
552 **100**, 607-20 (2016).  
553 20. Benjdia, A. et al. The thiostrepton A tryptophan methyltransferase TsrM catalyses a  
554 cob(II)alamin-dependent methyl transfer reaction. *Nat. Commun.* **6**, 8377 (2015).  
555 21. Pierre, S. et al. Thiostrepton tryptophan methyltransferase expands the chemistry of radical  
556 SAM enzymes. *Nat. Chem. Biol.* **8**, 957-9 (2012).  
557 22. Parent, A. et al. The B12-radical SAM enzyme PoyC catalyzes valine C-beta-methylation  
558 during polytheonamide biosynthesis. *J. Am. Chem. Soc.* **138**, 15515-15518 (2016).  
559 23. Freeman, M.F., Helf, M.J., Bhushan, A., Morinaka, B.I. & Piel, J. Seven enzymes create  
560 extraordinary molecular complexity in an uncultivated bacterium. *Nat Chem* **9**, 387-395 (2017).

- 561 24. Benjdia, A. et al. Insights into the catalysis of a lysine-tryptophan bond in bacterial peptides by  
562 a SPASM domain radical S-adenosylmethionine (SAM) peptide cyclase. *J. Biol. Chem.* **292**,  
563 10835-10844 (2017).
- 564 25. Balty, C. et al. Ruminococcin C, an anti-clostridial sactipeptide produced by a prominent  
565 member of the human microbiota *Ruminococcus gnavus*. *J Biol Chem* **294**, 14512-14525  
566 (2019).
- 567 26. Benjdia, A. et al. Insights into the catalysis of a lysine-tryptophan bond in bacterial peptides by  
568 a SPASM domain radical S-adenosylmethionine (SAM) peptide cyclase. *J Biol Chem* **292**,  
569 10835-10844 (2017).
- 570 27. Dowling, D.P. et al. Radical SAM enzyme QueE defines a new minimal core fold and metal-  
571 dependent mechanism. *Nat Chem Biol* **10**, 106-12 (2014).
- 572 28. Goldman, P.J., Grove, T.L., Booker, S.J. & Drennan, C.L. X-ray analysis of butirosin  
573 biosynthetic enzyme BtrN redefines structural motifs for AdoMet radical chemistry. *Proc Natl*  
574 *Acad Sci U S A* **110**, 15949-54 (2013).
- 575 29. Davis, K.M. et al. Structures of the peptide-modifying radical SAM enzyme SuiB elucidate the  
576 basis of substrate recognition. *Proc Natl Acad Sci U S A* (2017).
- 577 30. Grove, T.L. et al. Structural Insights into Thioether Bond Formation in the Biosynthesis of  
578 Sactipeptides. *J. Am. Chem. Soc.* **139**, 11734-11744 (2017).
- 579 31. Vey, J.L. & Drennan, C.L. Structural insights into radical generation by the radical SAM  
580 superfamily. *Chem Rev* **111**, 2487-506 (2011).
- 581 32. Haft, D.H. & Basu, M.K. Biological systems discovery in silico: radical S-adenosylmethionine  
582 protein families and their target peptides for posttranslational modification. *J. Bacteriol.* **193**,  
583 2745-55 (2011).
- 584 33. Benjdia, A. et al. Anaerobic sulfatase-maturing enzyme--a mechanistic link with glyceryl  
585 radical-activating enzymes? *FEBS J* **277**, 1906-20 (2010).
- 586 34. Grell, T.A.J. et al. Structural and spectroscopic analyses of the sporulation killing factor  
587 biosynthetic enzyme SkfB, a bacterial AdoMet radical sactisynthase. *J. Biol. Chem.* (2018).
- 588 35. Grell, T.A., Goldman, P.J. & Drennan, C.L. SPASM and twitch domains in S-  
589 adenosylmethionine (SAM) radical enzymes. *J. Biol. Chem.* **290**, 3964-71 (2015).
- 590 36. Broderick, J.B., Duffus, B.R., Duschene, K.S. & Shepard, E.M. Radical S-adenosylmethionine  
591 enzymes. *Chem Rev* **114**, 4229-317 (2014).
- 592 37. Tao, L., Zhu, W., Klinman, J.P. & Britt, R.D. Electron Paramagnetic Resonance Spectroscopic  
593 Identification of the Fe-S Clusters in the SPASM Domain-Containing Radical SAM Enzyme  
594 PqqE. *Biochemistry* **58**, 5173-5187 (2019).
- 595 38. Zhu, W. et al. Structural Properties and Catalytic Implications of the SPASM Domain Iron-  
596 Sulfur Clusters in *Methylorubrum extorquens* PqqE. *J Am Chem Soc* **142**, 12620-12634 (2020).
- 597 39. Yokoyama, K., Ohmori, D., Kudo, F. & Eguchi, T. Mechanistic study on the reaction of a radical  
598 SAM dehydrogenase BtrN by electron paramagnetic resonance spectroscopy. *Biochemistry* **47**,  
599 8950-60 (2008).
- 600 40. Blaszczyk, A.J. et al. Spectroscopic and Electrochemical Characterization of the Iron-Sulfur  
601 and Cobalamin Cofactors of TsrM, an Unusual Radical S-Adenosylmethionine Methylase. *J Am*  
602 *Chem Soc* **138**, 3416-26 (2016).
- 603 41. Weerasinghe, N.W., Habibi, Y., Uggowitz, K.A. & Thibodeaux, C.J. Exploring the  
604 Conformational Landscape of a Lanthipeptide Synthetase Using Native Mass Spectrometry.  
605 *Biochemistry* **60**, 1506-1519 (2021).
- 606 42. Benjdia, A. et al. Thioether bond formation by SPASM domain radical SAM enzymes: C $\alpha$   
607 H-atom abstraction in subtilosin A biosynthesis. *Chem Commun (Camb)* **52**, 6249-6252 (2016).
- 608 43. Morinaka, B.I. et al. Radical S-adenosyl methionine epimerases: regioselective introduction of  
609 diverse D-amino acid patterns into peptide natural products. *Angew Chem Int Ed Engl* **53**, 8503-  
610 7 (2014).
- 611 44. Dathe, M. & Wieprecht, T. Structural features of helical antimicrobial peptides: their potential  
612 to modulate activity on model membranes and biological cells. *Biochim Biophys Acta* **1462**, 71-  
613 87 (1999).

- 614 45. Ayikpoe, R. et al. Spectroscopic and Electrochemical Characterization of the Mycofactocin  
615 Biosynthetic Protein, MftC, Provides Insight into Its Redox Flipping Mechanism. *Biochemistry*  
616 **58**, 940-950 (2019).
- 617 46. Balo, A.R. et al. Trapping a cross-linked lysine-tryptophan radical in the catalytic cycle of the  
618 radical SAM enzyme SuiB. *Proc Natl Acad Sci U S A* **118**(2021).
- 619 47. Brito, J.A., Denkmann, K., Pereira, I.A., Archer, M. & Dahl, C. Thiosulfate dehydrogenase  
620 (TsdA) from *Allochromatium vinosum*: structural and functional insights into thiosulfate  
621 oxidation. *J Biol Chem* **290**, 9222-38 (2015).
- 622 48. Nakamura, R., Hikita, M., Ogawa, S., Takahashi, Y. & Fujishiro, T. Snapshots of PLP-substrate  
623 and PLP-product external aldimines as intermediates in two types of cysteine desulfurase  
624 enzymes. *FEBS J* **287**, 1138-1154 (2020).
- 625 49. Denisov, I.G., Makris, T.M., Sligar, S.G. & Schlichting, I. Structure and chemistry of  
626 cytochrome P450. *Chem Rev* **105**, 2253-77 (2005).
- 627 50. Kudo, F., Hoshi, S., Kawashima, T., Kamachi, T. & Eguchi, T. Characterization of a radical S-  
628 adenosyl-L-methionine epimerase, NeoN, in the last step of neomycin B biosynthesis. *J Am*  
629 *Chem Soc* **136**, 13909-15 (2014).
- 630 51. Besandre, R.A. et al. HygY Is a Twitch Radical SAM Epimerase with Latent Dehydrogenase  
631 Activity Revealed upon Mutation of a Single Cysteine Residue. *J Am Chem Soc* **143**, 15152-  
632 15158 (2021).
- 633 52. Dong, S.H., Liu, A., Mahanta, N., Mitchell, D.A. & Nair, S.K. Mechanistic Basis for Ribosomal  
634 Peptide Backbone Modifications. *ACS Cent Sci* **5**, 842-851 (2019).
- 635 53. Zhao, G. et al. Structural Basis for a Dual Function ATP Grasp Ligase That Installs Single and  
636 Bicyclic omega-Ester Macrocycles in a New Multicore RiPP Natural Product. *J Am Chem Soc*  
637 **143**, 8056-8068 (2021).
- 638 54. Song, I. et al. Molecular mechanism underlying substrate recognition of the peptide  
639 macrocyclase PsnB. *Nat Chem Biol* **17**, 1123-1131 (2021).
- 640 55. Miller, F.S. et al. Conformational rearrangements enable iterative backbone N-methylation in  
641 RiPP biosynthesis. *Nat Commun* **12**, 5355 (2021).
- 642 56. Fyfe, C.D. et al. Crystallographic snapshots of a B12-dependent radical SAM methyltransferase.  
643 *Nature* **602**, 336-342 (2022).
- 644 57. Krissinel, E. & Henrick, K. Inference of macromolecular assemblies from crystalline state. *J*  
645 *Mol Biol* **372**, 774-97 (2007).

646

647

## 648 **Methods**

### 649 **Cloning of EpeE D210A and Y2F-Y209F mutants**

650 The EpeE tyrosine mutants were obtained by site-directed mutagenesis with the plasmid pET28-Strep-TEV-EpeE used as DNA  
651 template. To generate the Y2F-Y209F mutant the following primers were used: 5'-CAT ATG TTC AAC AAA ACC GTG  
652 AGC-3' ; 5'-TCC GGG TTT CGA TAT TGT GTA TCA TC-3' ; 5'-ACA ATA TCG AAA CCC GGA CAA TGC AG-3'.  
653 PCR reactions typically contained 1  $\mu$ M of each primer, 250  $\mu$ M of each dNTP, 1  $\mu$ l of High Fidelity Polymerase (Thermo),  
654 ~50 ng DNA template and performed using the following PCR cycling parameters: 1 cycle at 95°C for 2 min followed by 36  
655 cycles of 95°C for 30 sec (denaturation), 55-60°C for 30 sec (hybridation), 72°C for 90 s (extension) and 1 cycle at 72°C for  
656 10 min. PCR products were purified on 1-2% agarose gel, digested with NdeI and XhoI (NEB), purified and ligated into  
657 NdeI/XhoI digested pET28-Strep-TEV plasmid. The D210A mutant gene was synthesis by GeneCust and ligated in plasmid  
658 pET28. The ligation products were transformed into chemically competent *E. coli* BL21 (DE3) star strain. Clones were selected  
659 on LB agar plate containing 50  $\mu$ g.mL<sup>-1</sup> kanamycine. One clone was selected after we checked the sequence of the targeted  
660 gene by DNA sequencing.

661

### 662 **Protein purification**

663 The constructs of wild-type and C223A mutant streptavidin-tagged EpeE were the same as previously published<sup>9</sup>. All  
664 recombinant proteins were overexpressed and purified as follows. Typically, 9 L of *E. coli* BL21 cells transformed with pET28  
665 plasmid containing the construct were grown in Luria-Broth (LB) media at 37°C with 50  $\mu$ g/mL Kanamycin, and protein  
666 expression induced at Abs<sub>600nm</sub> ~ 0.6 with 700  $\mu$ M IPTG. Overexpression was conducted overnight and cells resuspended in  
667 Buffer A (500 mM NaCl, 50 mM TrisHCl, pH 8.0) containing 0.5% Triton X-100, protease inhibitors and sonicated for 4 min  
668 on ice. Cell debris were pelleted by ultracentrifugation at 45,000 g (Beckman coulter) before loading supernatant on Streptactin  
669 resin (IBA) equilibrated in buffer A. After washing in buffer A, the recombinant protein was eluted with buffer A supplemented  
670 by 3 mM desthiobiotin. Protein was aliquoted, flash frozen in liquid N<sub>2</sub> and stored at -80°C. Concentration was measured by  
671 absorbance at 280 (using ProtParam calculated  $\epsilon$  and molecular weights) and purity assessed by SDS-PAGE on 12% gels and  
672 PageBlue staining.

673

### 674 **Iron sulfur clusters reconstitution**

675 *In vitro* reconstitution of the EpeE [4Fe-4S] clusters was achieved in presence of 3 mM DTT by addition of 8 molar excess of  
676 (NH<sub>4</sub>)<sub>2</sub>Fe(SO<sub>4</sub>)<sub>2</sub> and Na<sub>2</sub>S. After incubation under anaerobic atmosphere, excess of unbound iron and sulfur was removed onto  
677 a desalting column against buffer A with 3 mM DTT. Reconstitution of the protein was verified by recording UV-visible spectra  
678 (250-700 nm).

679

### 680 **Peptide synthesis**

681 The EpeX peptide **1** and RiPP-fragments peptide **2** (KKEITNNETVKNLEFKGLLDESQKLAKVNDL), peptide **3**  
682 (KNLEFKGLLDESQKLAKVNDL), peptide **4** (WYFVKSKEN), peptide **5** (FVKSKENRWIL), peptide **6**  
683 (KENRWILGSGH), peptide **7** (NRWILGSGH) were synthesized by solid-phase synthesis (ProteoGenix, France). In bold,  
684 residues targeted by EpeE.

685

### 686 **EPR analysis**

687 EPR samples were prepared immediately after reconstitution of the iron-sulfur clusters in the glove box. Reduction was  
688 achieved in 5 minutes by the addition of 3 mM sodium dithionite. Samples in the presence of SAM were prepared by addition  
689 of 3-5 fold stoichiometric excess of SAM. Samples were then frozen in liquid isopentane in the glove box and then maintained  
690 in liquid nitrogen until EPR measurements were performed. EPR spectra were recorded on a Bruker ElexSys-500 X-band  
691 spectrometer equipped with a standard rectangular cavity (ST4102) fitted to an Oxford Instruments liquid helium cryostat  
692 (ESR900) and temperature control system. The spectrometer settings were as follows: microwave frequency, 9.48 GHz,  
693 conversion time of 80 ms, modulation amplitude of 1 mT, and modulation frequency of 100 kHz. Other settings are given in  
694 the corresponding figure captions.

695 HYSCORE experiments were measured at 6 K using a Bruker EleXsys E580 spectrometer equipped with an ER4118X-MD5  
696 dielectric resonator and an Oxford Instruments CF 935 cryostat. This four-pulse experiment ( $\pi/2$ - $\tau$ - $\pi/2$ - $t_1$ - $\pi$ - $t_2$ - $\pi/2$ - $\tau$ -echo) was  
697 employed with an appropriate 8 step phase-cycling scheme to eliminate unwanted features from the experimental electron spin  
698 echo envelopes. The intensity of the echo after the fourth pulse was integrated over 32 ns with varied  $t_2$  and  $t_1$  and constant  $\tau$ .  
699 The length of a  $\pi/2$  pulse was 12 ns and of a  $\pi$  pulse 24 ns. A  $\tau$  value of 132 ns and a shot repetition rate of 1 kHz were used.  
700 HYSCORE data were collected in the form of 2D time-domain patterns containing 256  $\times$  256 points with steps of 16 ns. Spectra  
701 were recorded at the magnetic field value corresponding to the maximum absorption of the [4Fe-4S]<sup>1+</sup> signal in the absence of  
702 SAM (corresponding to  $g = 1.929$ ). HYSCORE spectra were processed using Bruker's Xepr software. Relaxation decays were  
703 subtracted (fitting by 3<sup>rd</sup> order polynomial functions) followed by zero-filling to 1024 points and tapering with a Hamming  
704 window, before 2D Fourier transformation which finally gives the spectrum in frequency domain. Processed data were then  
705 imported into Matlab (The MathWorks Inc., Natick, MA) for plotting. HYSCORE spectra are shown in absolute value mode  
706 and are presented as contour plots.

707

### 708 **Enzyme assay**

709 The activity of EpeE towards the synthetic peptides was assayed in deuterated buffer (150 mM KCl, 25 mM TrisDCl, pH 8.0,  
710 DTT 3 mM); all compounds were dissolved in D<sub>2</sub>O and the reconstituted protein was buffer exchanged against deuterated  
711 buffer. EpeE (235  $\mu$ M) was incubated with 3 mM DTT, 3 mM SAM and 2.25 mM peptide. The reactions were initiated by  
712 addition of 3 mM sodium dithionite.

713 For the kinetic experiments, the EpeE WT, C223A, D210A and Y2F-Y209F mutants (100 $\mu$ M) were incubated with 1 mM  
714 SAM, 500 $\mu$ M peptide 6 and reactions were initiated with the addition of flavodoxin/flavodoxin reductase and 2.7 mM NADPH.  
715 All reactions were performed at 25°C and 15  $\mu$ L aliquots sampled overtime for LC-MS/MS analysis.  
716

#### 717 **Liquid chromatography–mass spectrometry/mass spectrometry analysis**

718 LC-MS/MS analysis were achieved using a Q-Exactive Focus mass spectrometer (ThermoFisher Scientific) with the HESI2  
719 electrospray ion source associated to a Vanquish Flex LC system (Thermo Fisher Scientific). Molecule separation was  
720 performed on a Zorbax Eclipse Plus C18 column (2.1X50mm, 1.8 $\mu$ m, RRHT, Agilent). Samples were dilute one hundred time  
721 before injection with TFA 0.1% or in acetonitrile 50%, to discard the protein by precipitation. Peptides 4, 5, 6 or 7 were eluted  
722 on the reverse phase column by an acetonitrile gradient with formic acid 0.1% as ion pairing agent and detected by mass  
723 spectrometry in positive mode. The doubly charged ions corresponding to the peptides 4, 5, 6, 7 were selected for HCD  
724 fragmentation step at 35 % or 20 % of NCE. For detection and quantitation of the epimerized peptide 5 by mass spectrometry,  
725 the samples were hydrolyzed using trypsin Promega (V5111) to produce the peptide fragment WILGSGH and extract the  
726 corresponding MS signal of the doubly charge ion (385.21<sup>2+</sup>). This method enables us to quantify the epimerized and  
727 unmodified peptides. Unmodified peptide fragment eluted at 13.7 min and the epimerized fragment at 18.2 min from the  
728 column. The 5'-dA produced during *in vitro* reactions with EpeE (wild-type and D210A, C223A and Y2F-Y209F mutants) was  
729 quantified in the sample by mass spectrometry using a direct standard curve of 5'-dA.  
730

#### 731 **Crystallization of EpeE, EpeE C223A, EpeE D210A mutants and complexes with peptides 5 and 6**

732 For crystallization purposes, the freshly reconstituted protein was further purified by size exclusion on a Superdex-200 10/300  
733 GL Increase column (Äkta system, GE Healthcare) to achieve homogeneity in the protein preparation. Protein was then  
734 typically concentrated to 20 mg/mL before setting up crystallization experiments. Crystals were obtained by using the sitting  
735 drop vapor diffusion technique at 21°C under anaerobic atmosphere. After several rounds of optimization, brown rod shaped  
736 single crystals were obtained in 3 % Ethylene Glycol, 9.6 % PEG 8,000, 0.1 M HEPES pH 7.5, with a 2:1 protein:mother liquor  
737 ratio, and were used for anomalous data collection (**EpeE phasing dataset, Extended Table 1**). EpeE wild-type crystals (**EpeE**  
738 **WT, Extended Table 1**) appeared within 24 h by using hanging drop diffusion and a 1:1 mixing of protein (7.5 mg ml<sup>-1</sup> with  
739 0.5 mM SAH) and precipitant solution (0.1 M Tris-HCl pH 8.5, 17.5 % polyethylene glycol (PEG) 1,000). EpeE D210A mutant  
740 crystals (**EpeE D210A, Extended Table 1**) were grown in same conditions as EpeE WT in presence of SAH. EpeE C223A  
741 mutant crystals (**EpeE C223A, Extended Table 1**) were grown in 2:1 drops mixing protein (10 mg ml<sup>-1</sup> with 1 mM SAM) and  
742 precipitant solution. The crystals of complexes from EpeE wild-type (**EpeE WT peptide 5, Extended Table 1**) and EpeE  
743 C223A mutant (**EpeE C223A peptide 5, EpeE C223A peptide 6, Extended Table 1**) were obtained mixing precipitants (0.1  
744 M Tris-HCl pH 8.5, 14-20% PEG 1,000) with protein, SAH (0.5 mM) and peptide (5 mM). All crystals were typically obtained  
745 within 24 hours under anaerobic atmosphere and flash cooled in liquid N<sub>2</sub> under anaerobic conditions.  
746

#### 747 **Crystallographic structure determinations**

748 X-ray diffraction data were recorded on PROXIMA-1 beamline at Synchrotron SOLEIL<sup>58</sup>, equipped with a Pilatus-6M hybrid  
749 pixel detector<sup>59</sup> and a three-axis SmarGon goniometer. An X-ray energy of 7.14 keV was chosen for the single anomalous  
750 phasing experiments, for which two sets of images were recorded at two different Chi angles to favor obtaining a more complete  
751 merged data at 2.99 Å resolution. The X-ray energy was 12.67 keV for subsequent data collection. For the experimental phasing  
752 measurements, the X-ray energy was attenuated to 5% of the beam intensity, providing with a flux of 1.0 x 10<sup>10</sup> photons.s<sup>-1</sup> at  
753 the sample position; the more standard data at 12.67 keV were recorded with 20% of the beam intensity. Phasing and data  
754 analysis and processing was performed using SHARP/AutoSHARP (SHARP 2.8.12 and Sushi 3.10.11), and the CCP4 suite  
755 (7.1.016). Data were processed with XDS 2022/01/10<sup>60</sup> through the *xdsme* scripting package<sup>61</sup>. The ( hkl ) and ( -h-k-l )  
756 reflections were treated separately in all steps, including scaling and merging. Data sets were scaled with XSCALE  
757 2022/01/10<sup>60</sup>, converted to MTZ format with POINTLESS 1.12.13<sup>62</sup> and merged with AIMLESS 0.7.8<sup>63</sup>, as implemented within  
758 the *xdsme* automated procedure.

759 For the EpeE phasing dataset, structure-factor amplitudes were obtained with TRUNCATE 8.0.010<sup>64</sup>. The Matthews coefficient  
760 suggested that the crystal contained two monomers *per* asymmetric unit. Four iron cluster sites were located with SHELXC/D  
761 2016/1<sup>65</sup>, and their respective positions were refined with SHELXE 2019/1 (through HKL2MAP)<sup>66</sup> and Phaser 2.8<sup>67</sup>. Initial  
762 correct substructures were determined immediately with SHELXD 2013/2, with two well-separated clusters in the plot of CC<sub>all</sub>  
763 versus CC<sub>weak</sub>. The phase information was improved using the existing non-crystallographic symmetry (NCS) between the two  
764 molecules within the asymmetric unit. One helix surrounding the iron clusters was docked in the original electron density using  
765 Coot<sup>68</sup> to facilitate the calculation of the matrix. Given this matrix, Phaser unequivocally identified the rotation and translation  
766 parameters of two monomers and confirmed the space group P2<sub>1</sub>2<sub>1</sub>2<sub>1</sub>. Side chains were placed by automated model building  
767 with Buccaneer 1.6.12/REFMAC5<sup>69</sup>. Missing residues, water molecules and ligands were fitted in the 2F<sub>o</sub>-F<sub>c</sub> and F<sub>o</sub>-F<sub>c</sub>  
768 electron-density maps using Coot. For structure refinements of the subsequent models, phases were introduced from the original  
769 structure as a template coordinates (Phaser) and the structures were refined iteratively with REFMAC5 or BUSTER (version  
770 2.10.4)<sup>70</sup>. Manual building was performed with Coot (version 0.9.6.1.1). The structures were validated by MolProbity as  
771 implemented in phenix version 1.19.2-4158<sup>71</sup>. Data collection and refinement statistics are shown in Extended Table 1. All  
772 structural representations were generated with PyMOL v0.99 (DeLano Scientific LLC) or PyMOL v2.5 (Schrödinger, LLC).  
773

#### 774 **SEC-SAXS data measurement**

775 All the data was collected in SEC-SAXS mode with an in-line Superdex 200 Increase 5/150 GL column (GE Healthcare).  
776 Homogeneous reconstituted proteins were loaded on our anaerobic setup which was based on an HPLC system equilibrated  
777 with degassed buffer containing 1 mM DTT and an auto-sampler flushed by a continuous flux of N<sub>2</sub>. The SAXS data was  
778 collected at the SWING beamline at the SOLEIL synchrotron, France, equipped with an Eiger 4M detector with a sample-to-



779 detector distance of 2 m<sup>2</sup>. The parameters used for SAXS data collection are given in **Supplementary Table 10**. More  
780 information is available in **Supplementary Table 10**.

781

### 782 **Reporting summary**

783 Further information on research design is available in the Nature Research Reporting Summary linked to this paper.

### 784 **Data Availability**

785 Atomic coordinates and structure factors for the reported crystal structures in this work have been deposited in the Protein Data  
786 Bank upon accession codes: 8AI1, 8AI2, 8AI3, 8AI4, 8AI5 & 8AI6. SAXS data have been deposited in the Small Angle  
787 Scattering Biological Data Bank upon accession codes SASDRS7, SASDRR7. The data for this study are available within the  
788 paper and its Supplementary Information. Source data are provided with this paper.

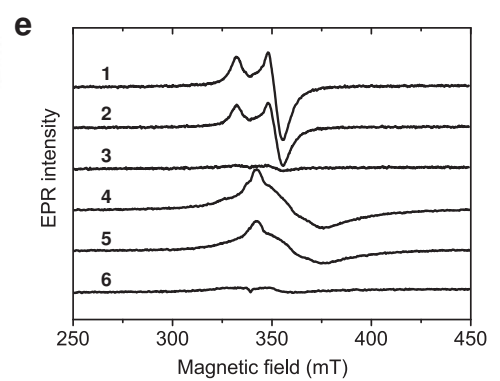
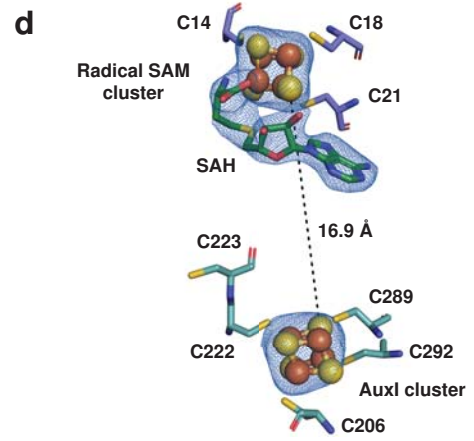
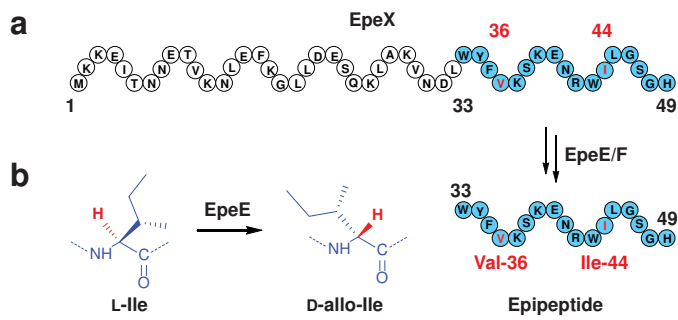
789

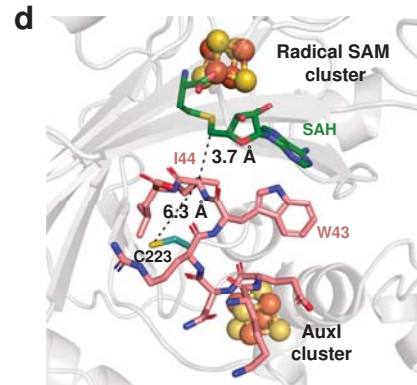
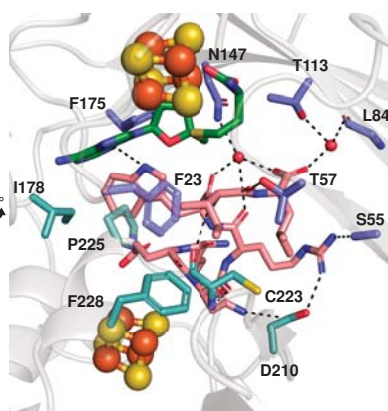
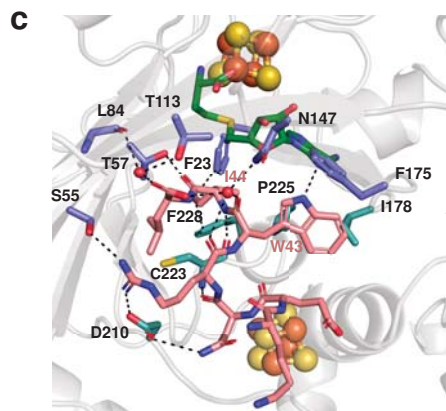
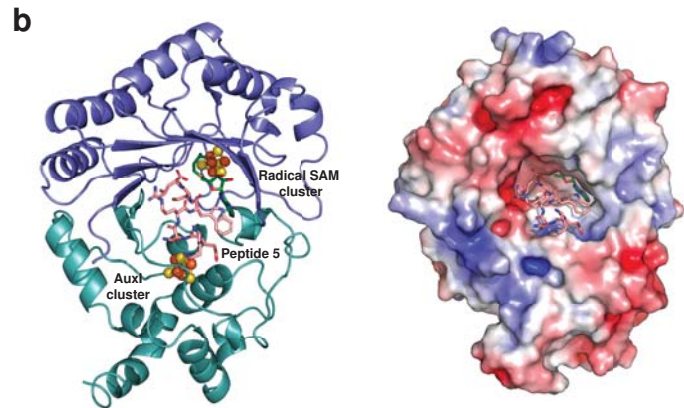
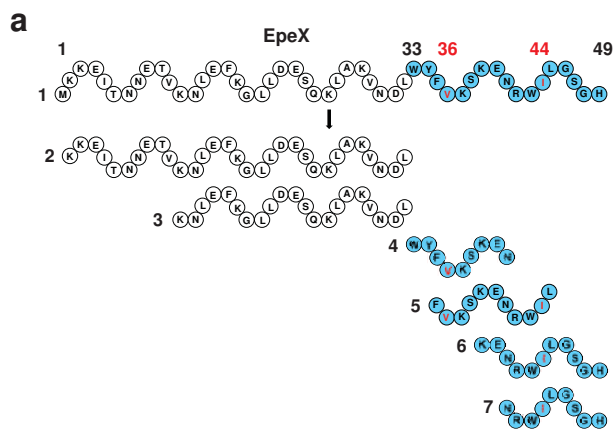
## 790 **References**

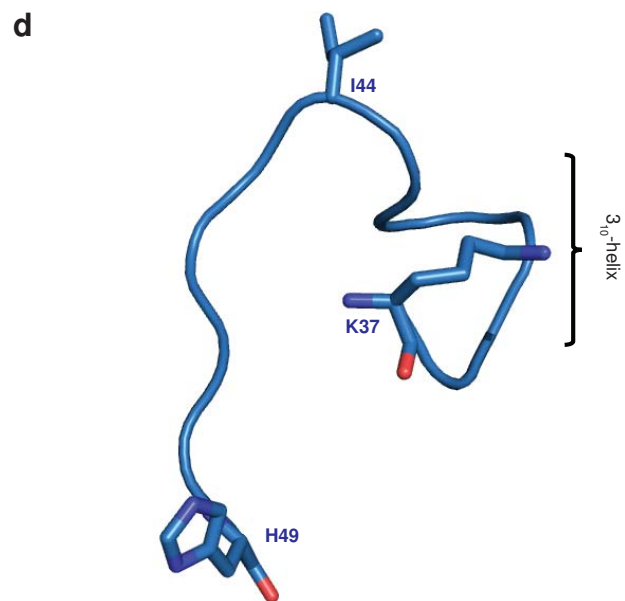
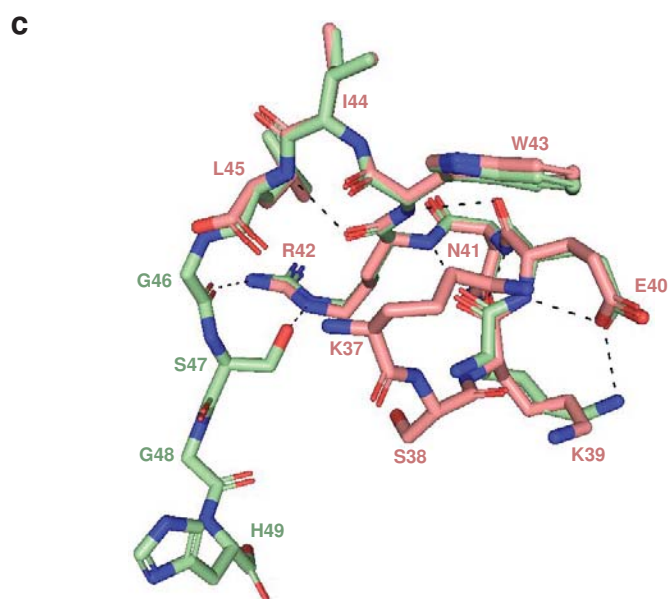
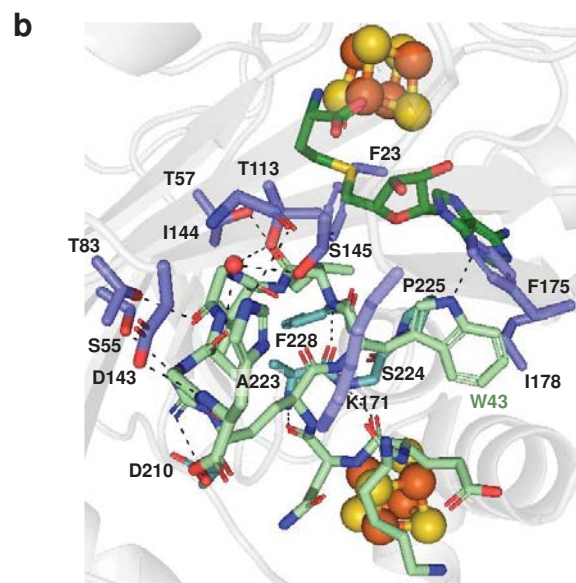
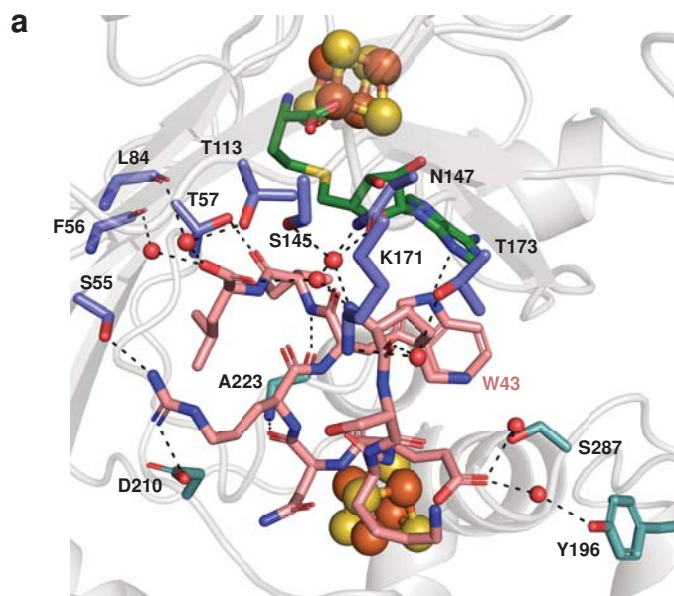
791

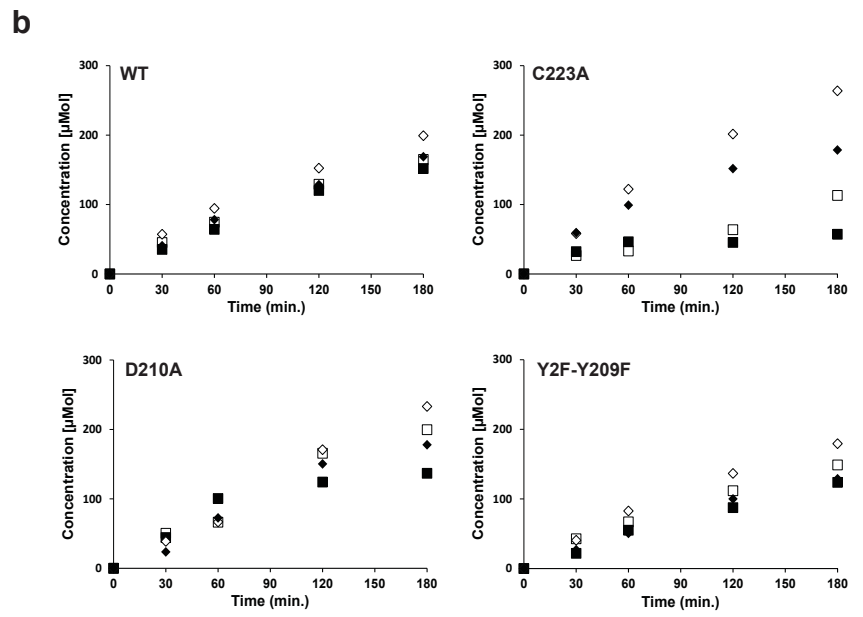
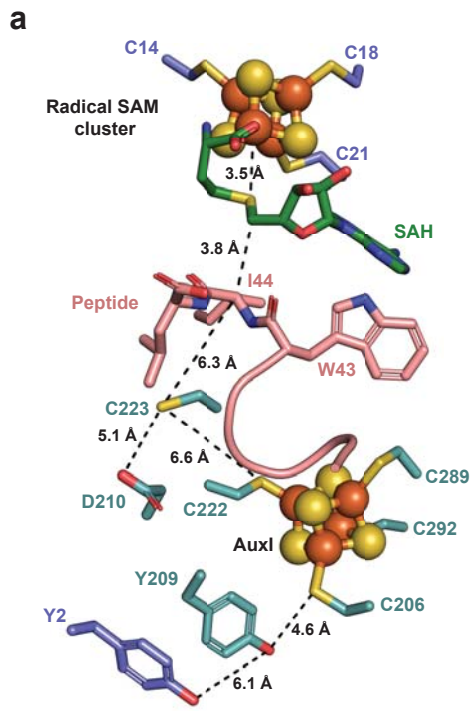
- 792 58. Coati, A. et al. Status of the crystallography beamlines at synchrotron SOLEIL\*. *The European Physical Journal Plus*  
793 **132**(2017).
- 794 59. Kraft, P. et al. Performance of single-photon-counting PILATUS detector modules. *Journal of Synchrotron Radiation*  
795 **16**, 368-375 (2009).
- 796 60. Kabsch, W. XDS. *Acta Crystallographica Section D Biological Crystallography* **66**, 125-132 (2010).
- 797 61. Legrand, p. XDSME: XDS Made Easier. GitHub repository (2017).
- 798 62. Evans, P. Scaling and assessment of data quality. *Acta Crystallographica Section D Biological Crystallography* **62**, 72-  
799 82 (2006).
- 800 63. Evans, P.R. & Murshudov, G.N. How good are my data and what is the resolution? *Acta Crystallographica Section D*  
801 *Biological Crystallography* **69**, 1204-1214 (2013).
- 802 64. Winn, M.D. et al. Overview of the CCP 4 suite and current developments. *Acta Crystallographica Section D Biological*  
803 *Crystallography* **67**, 235-242 (2011).
- 804 65. Sheldrick, G.M. A short history of SHELX. *Acta Crystallogr A* **64**, 112-22 (2008).
- 805 66. Pape, T. & Schneider, T.R. HKL2MAP : a graphical user interface for macromolecular phasing with SHELX programs.  
806 *Journal of Applied Crystallography* **37**, 843-844 (2004).
- 807 67. McCoy, A.J. et al. Phaser crystallographic software. *Journal of Applied Crystallography* **40**, 658-674 (2007).
- 808 68. Emsley, P., Lohkamp, B., Scott, W.G. & Cowtan, K. Features and development of Coot. *Acta Crystallographica Section*  
809 *D Biological Crystallography* **66**, 486-501 (2010).
- 810 69. Murshudov, G.N. et al. REFMAC 5 for the refinement of macromolecular crystal structures. *Acta Crystallographica*  
811 *Section D Biological Crystallography* **67**, 355-367 (2011).
- 812 70. Smart, O.S. et al. Exploiting structure similarity in refinement: automated NCS and target-structure restraints in BUSTER.  
813 *Acta Crystallographica Section D Biological Crystallography* **68**, 368-380 (2012).
- 814 71. Chen, V.B. et al. MolProbity : all-atom structure validation for macromolecular crystallography. *Acta Crystallographica*  
815 *Section D Biological Crystallography* **66**, 12-21 (2010).
- 816 72. Thureau, A., Roblin, P. & Perez, J. BioSAXS on the SWING beamline at Synchrotron SOLEIL. *Journal of Applied*  
817 *Crystallography* **54**, 1698-1710 (2021).

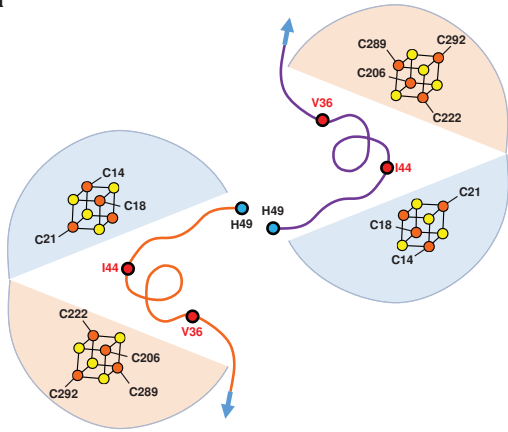
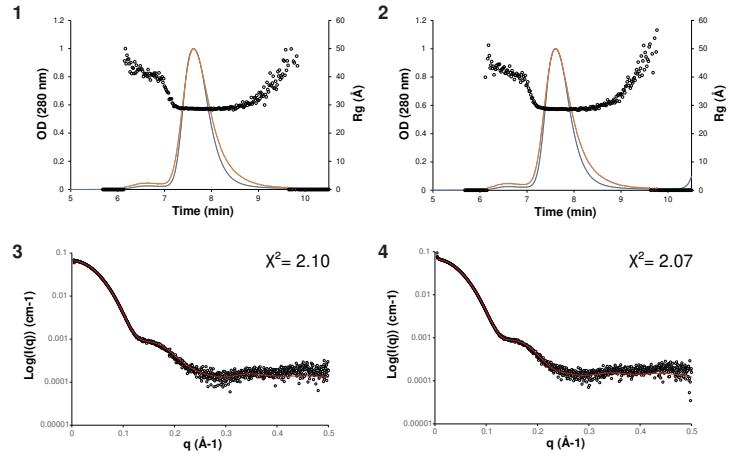
818









**a****b****c**